Developing state of the art sample preparation for high resolution electron microscopy

A report submitted to TCD, School of Chemistry for Research master's MSc

Author: Clive Downing

Supervisor: Prof. Valeria Nicolosi

2020

Declaration of Authorship

I declare that this thesis has not been submitted as an exercise for a degree at this or any other university and it is entirely my own work.

I agree to deposit this thesis in the University's open access institutional repository or allow the Library to do so on my behalf, subject to Irish Copyright Legislation and Trinity College Library conditions of use and acknowledgement.

_____

Clive Downing

Summary

In this work, a range of ion species interactions with silicon were investigated to find the most suitable ion species and operating parameters to produce samples suitable for high-resolution electron microscopy and spectroscopy. Cross-sections of the ion beam interactions were imaged using electron microscopy to visualise any structural damage caused to the single crystal silicon after ion bombardment. Computer simulations were also performed to help understand and back up the data from the imaging. A new technique was developed using a commercially available low energy argon ion milling instrument allowing the efficient preparation of ultra-thin damage-free samples from which high-resolution imaging and spectroscopy were successfully performed.

Summary

Acknowledgements

I would sincerely like to thank my supervisor Prof. Valeria Nicolosi for all her help and support.

A special thank you to Don Ashcroft, for taking a gamble on a young lad working in a music shop and introducing him (me) to science.

A massive thank you to Pierce, Eoin and Megan for guidance and support. I would also like to thank to Dermot, Cathal, Jakub, Lewys and Aleksey, for all help along the way

Finally, I would like to say a huge thanks to my awesome girlfriend Louise and little dog Molly for being there, supporting me and generally putting up with me during the writing process.

Contents

1 Introduction

Material characterisation is key to understanding the fundamental properties of the world around us. From the macro-to-nano scale, the direct visualisation of a material's structure has allowed us to gain a handle on material design, critical to their use in applications. Microscopy has led this area, with techniques such as electron microscopy (EM) capable of providing atomic scale imaging and analysis, giving an insight into the behaviour of individual atoms [1]. The main challenge in any microscopy technique is to prepare a specimen that is representative of the material under investigation. In this era of high-resolution, low voltage electron microscopes with instruments capable of resolving tens of picometers and able to perform high-resolution spectroscopy, sample preparation is key to being able to obtain viable results. Sample preparation for electron microscopy has never been a trivial task. One of the big problems to overcome is producing samples thin enough while still maintaining their integrity. Even the best instruments in the world cannot perform without a well-prepared sample, but now the demands are greater than ever. In recent years with the aid of complex aberration correctors, transmission electron microscopes (TEM) have been capable of high-resolution imaging at scanning electron microscope (SEM) voltages (30kV-40kV). The resolution of electron energy loss spectroscopy (EELS), a technique widely used for elemental and chemical analysis, has improved dramatically going from hundreds of meV down to as low as 5 meV spectral resolution. This high-resolution spectroscopy can only be unlocked with the correct samples or sample preparation. If a sample is too thick the plural scattering through the bulk of the sample will hide any details in the plasmon region of the spectrum, as explained later.

Traditionally samples have been prepared by mechanical thinning, chemical thinning and even breaking up crystals using a pestle and mortar. Another approach to producing thin samples is to use a beam of ions [2]. Ions are much heavier than electrons so when accelerated at a surface they will displace atoms and remove material. A focused Ion beam microscope (FIB) can use this destructive interaction to make precise localised cuts into the surface of a bulk sample. The aim of this research is to investigate different ion species interactions with an end goal of improving sample quality for high-end electron microscopy characterisation.

FIB has become a standard technique for cross-section preparation For TEM imaging and analysis [3] [4]. These TEM cross-section samples are known as lamellae. In the past FIB was only really used where targeted sample preparation was needed; this is mainly due to the fact that older instruments operated at a fixed 30kV and used an unreliable ex-situ lift-out procedure for the transfer of lamella to the TEM grid. The modern FIB has come a long way: a system equipped with a nano manipulator allows for full *in-situ* lamella preparation, including low voltage thinning. FIB's generally use a heavy Ga^+ ion source, and even at low voltage this can cause damage to the sample [5], the heavy ions can disrupt crystal structure and even turn a crystalline area completely amorphous. For years mechanically polished samples have been post-processed with Ar^+ ion beam; these broad ion beam systems have also been used for post-processing of FIB lamellae. One of the drawbacks is the large interaction area, where unwanted thinning can occur in areas that you do not want to thin. Recently we have seen light ion species microscopes become commercially available. The Zeiss NanoFab [6] uses He and Ne ions and even includes a Ga^+ column, primarily the He ion system was developed for imaging purposes but has also been used for nanofabrication. The He^+ and Ne^+ ions are very light and have a low sputter yield. This may seem like the perfect solution for fine detailed finishing of the lamella in preparation for high-resolution low voltage imaging and spectroscopy. This research will investigate these light ion-matter interactions with the end goal of producing high-quality samples for high-end EM analysis.

2 EM Theory

So why are we using electrons anyway? If a single stream of photons could be fired in a straight line, infinitely small features could be resolved. However, due to the wave-like nature of light, we are actually limited by diffraction, which in turn limits the size of the features that can be resolved. Any optics system is ultimately limited by diffraction. This effect can be observed when the size of the aperture is reduced down to the physical size of the wavelength of the source; at this point, single slit interference effects can be seen in the probe and, as the aperture is reduced further, the scattering effects increase, reducing resolution. The formula, shown in eq. 1 below, published in 1873 by Ernst Abbe can be used to calculate the smallest resolvable distance d, limited by diffraction for a perfect optical system with no aberrations [7].

$$d = \frac{\lambda}{2NA} \qquad\qquad eq.1$$

Where λ is wavelength and NA is numerical aperture. Numerical aperture (NA= $n * \sin\theta$) is the angle of the beam in relation to the objective lens; n is the refractive index of the medium between the sample and the objective lens, air/vacuum is approximately 1.

Figure 1 shows the effect of a beam passing through a small aperture. The diffracted beam produces a pattern known as the 'Airy disk', figure 1(a). The combination of λ and NA defines the minimum spot size and, hence, defines the optical system's smallest differentiable distance as the maxima of two neighbouring Airy disks overlap. The radius of the central maxima is defined in eq. 2.
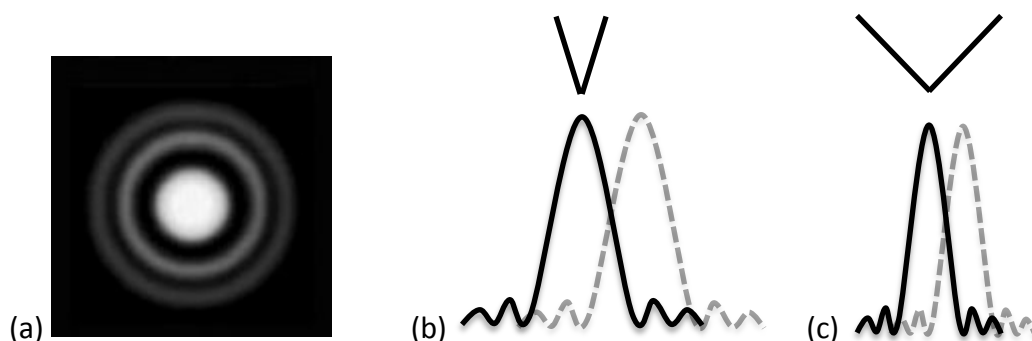

(a)   (b)   (c)

Figure 1: (a), As a wave front passes through a small aperture, the effects of diffraction are observed this is known as an Airy pattern. (b) and (c) diagram displaying the effects of beam convergence angle on the profile of an Airy disc

$$r = \frac{0.61\lambda}{NA} \qquad\qquad eq.\,2$$

The radius of the central maxima of the Airy disc r can be calculated using the Rayleigh criterion eq.2, where λ is wavelength and NA is the convergence angle of the probe. As the angle is increased the width of the central maxima decreases and the minimum resolvable between two points decreases this improves the resolution of the optical system, figure 1 (b), (c). After convergence angle has been optimised only decreasing wavelength will improve resolution.

An alternative to light (photons) is to use electrons to improve our microscopes resolution. Electrons can be accelerated at high voltages to produce far shorter wavelengths than light, resulting in improved resolution. If we consider De Broglie's equation eq. 3a,b below, we now have a equation to calculate the relationship between the electron wavelength and kinetic energy;

$$\lambda = \frac{h}{p} \qquad\qquad eq.\,3a$$

$$\lambda = \frac{h}{\sqrt{2m_e eE}} \qquad\qquad eq.\,3b$$

Where h is Planck's constant ($6.63{\times}10^{-34}$), p is Momentum, m_e is the Rest mass of an electron ($9.1{\times}10^{-31}$ kg), e is Electron charge ($1.6{\times}10^{-19}$ Coulombs) and E is accelerating voltage.

The shortest visible wavelength of light is violet at ~400nm, whereas an electron accelerated at 300kV is 0.002nm and if an accelerating voltage as low as 60kV is used, the wavelength is still only 0.005nm. This means that even working with a relatively low voltage for an electron microscope the wavelength is tens of thousands of times shorter than the shortest wavelength of light.

Modern electron microscopes allow sub-atomic size probes to be formed even at lower accelerating voltages (i.e. 30-40kV), enabling high-resolution imaging across a range of materials. This modern age of the electron microscopes has brought the technique far beyond just an imaging instrument in the area of metallurgy and materials science; it has become a high-resolution characterization instrument for all areas of science. When the electron beam interacts with the sample many other signals are generated. This enables more information to

be gained from the material the beam is interacting with. This allows elements and even their chemical states to be identified.
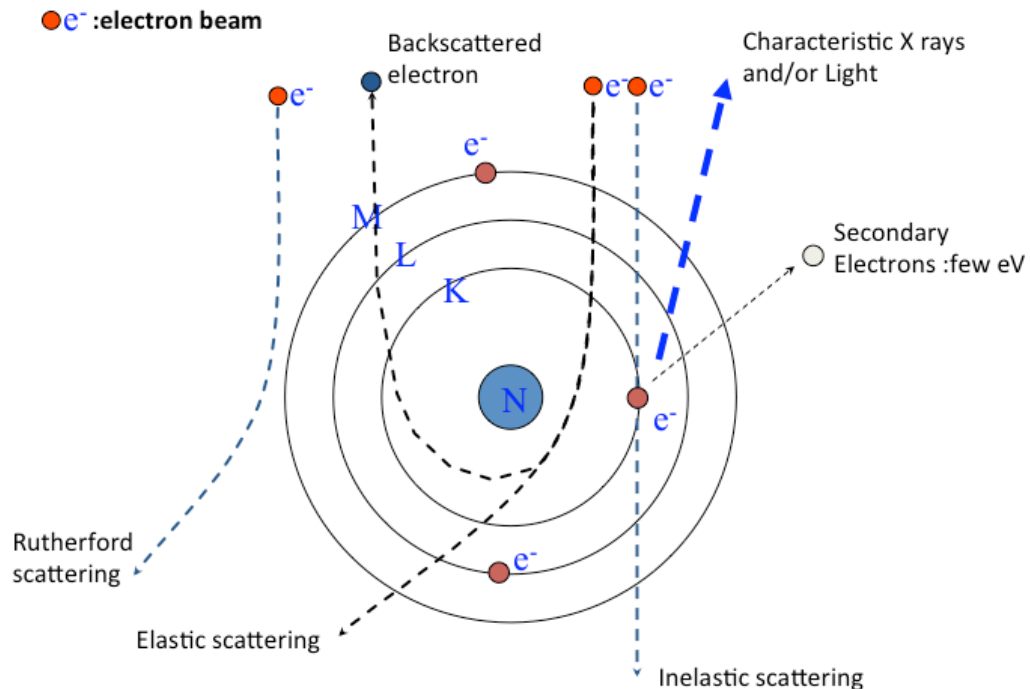

Figure 2: Displaying different electron interactions with an atom and the signals produced [8].

Figure 2 displays some of the interactions an electron can have with an atom. When performing electron microscopy two types of interaction are significant to us, elastic and inelastic interactions. Elastic scattering occurs when no energy is transferred from the incident beam to the atom and the electrons are scattered out like a pool ball bouncing off the edge of a pool table. The angle at which the electron scatters is related to the crystal structure of the material. This allows us to capture diffraction patterns and gain information about the crystal structure of the sample. Inelastic scattering occurs when the incident beam transfers part of its energy into the sample by interacting with the electron orbitals of the atoms. The incoming electron loses energy from this interaction, but does not move far from its original path resulting in low angle scattering. In terms of characterising materials via EM inelastic scattering is generally the most useful interaction because it generates the signals for energy dispersive X-ray (EDX) analysis and EELS. An inelastic scattering event occurs when the energetic beam removes a core-shell electron from its orbit around the nucleus; at this point the atom is left in an energised state, ionised, and wants to minimise its energy and return to its ground state. It

does this by transferring an outer shell electron to the hole in the core shell. This transfer causes energy to be released in the form of an x-ray, Auger electron [9]-p61 or photon (light). EDX analysis is used to measure the x-ray energy and identify elements in the specimen. Another consequence of this interaction is that the incident electron loses energy. An electron energy loss spectrometer is used to measure the energy lost during this interaction. In addition to elemental information it also provides an insight into how the atom is bonded to its neighbouring atoms, by giving chemical information such as oxidation states. However, there is a downside to inelastic scattering when an electron undergoes multiple inelastic scattering events. This is known as plural scattering. Plural scattering scales with sample thickness. This causes loss of information from EELS spectra, in particular in the low energy loss region. It also degrades image quality.

Another signal that is frequently used in transmission electron microscopy is generated by high angle Rutherford scattered electrons [10]. This signal is used for imaging and is collected using a high-angle annular dark field (HAADF) detector. HAADF imaging gives strong Z-contrast (where Z is the atomic number of the element considered). Therefore, from a single image it is possible to see where heavier and lighter elements are positioned. Rutherford scattering is a Coulomb interaction; an electrostatic interaction of an electron with the atom. HAADF imaging compliments EELS, as the annular detector collects electrons scattered out to high angles and the inelastic scattered electrons pass through the detector allowing them to be analysed by the EELS spectrometer. This enables simultaneous imaging and analysis.

We have discussed how electron microscopy is an extremely useful technique to record an image of a specimen. Also, by utilising the beam-specimen interaction we can measure the elemental and chemical composition through EDX and EELS. In the next section we extend our discussion and consider the interaction theory of ion beams with matter.

3   Ion interaction theory

Ions are atoms or molecules with a net charge resulting from the loss or gain of electrons. Having far greater mass than individual electrons, ions can be used to remove material efficiently at the nanoscale. Due to their greater mass, ions have significantly more momentum than electrons, so when an ion interacts with the sample it can physically remove atoms if the ion's energy is beyond a certain threshold. Like electrons, ions go through different types of interactions when accelerated at a sample, namely nuclear and electronic. The electronic interaction is an inelastic interaction where the charged particle excites electrons in the sample. This process emits secondary electrons from the sample surface, which we can then use for imaging. The incident ion only loses a small amount of energy during an electronic interaction and can go through many such events on its path. Nuclear interactions are where the ion physically knocks into the nucleus of an atom in the sample. This interaction can displace and remove atoms and ions from the sample. Through this type of interaction, the incident ions can lose a significant amount of energy. We are primarily interested in nuclear interactions for the fabrication of our samples.

Let us now consider the energy transferred during ion-sample collisions using eq. 4 below [11] [12]-p48.

$$T_m = E \frac{4M_1 M_2}{(M_1 + M_2)^2} \qquad\qquad eq.\,4$$

The maximum transferable energy, T_m , from a direct collision between a charged particle and an atom in the sample is related to the species' masses, where M_1 is the mass of the accelerated particle, M_2 is the mass of the target atom, and E is the energy of the accelerated particle in Joules. Applying eq. 4, we can calculate that a 30 keV electron can transfer 2.34 eV of its energy to a silicon atom, whereas a 30 keV Ga^+ ion can transfer over three orders of magnitude more energy at 24,540 eV. Each element has a threshold displacement value; the minimum energy that needs to be transferred to an atom to displace it from its position. Threshold displacement values are normally calculated from computational modelling using methods such as density functional theory (DFT). The value for silicon is ~25 eV, and from the values calculated above, we can see a 30 keV electron beam does not transfer enough energy to displace atoms, whereas a 30 keV Ga^+ ion beam has more than enough energy to displace

and remove silicon atoms. An electron would need to be accelerated to ~145 keV to have enough energy to displace a silicon atom.

Even light ions transfer significant energy to the specimen. Using eq. 4, we can calculate that a 30 keV He$^+$ ion can transfer up to 13,089 eV, which again is more than enough energy to displace a silicon atom. Compared to Ga$^+$ ions, light He$^+$ ions at 30 keV have significantly more velocity, causing the ion to travel further into the bulk, as the penetration depth, or stopping distance, directly relates to the velocity at which the ion is travelling.

The interactions between ions and a specimen during impact can be modelled using software such as SRIM (stopping range of ions in matter) [13]. SRIM is a Monte Carlo simulation using the BCA (binary collision approximation) which maps each ion's stopping distance and trajectory as it travels into the sample. The path of each ion is displayed in an image, and when enough ions have been simulated, the image provides an approximation of the interaction depth and volume for different ion species, at different accelerating voltages. Figure 3 shows two SRIM simulations I performed, for 100 ions of He$^+$ and Ga$^+$ accelerated at 30 keV into silicon.
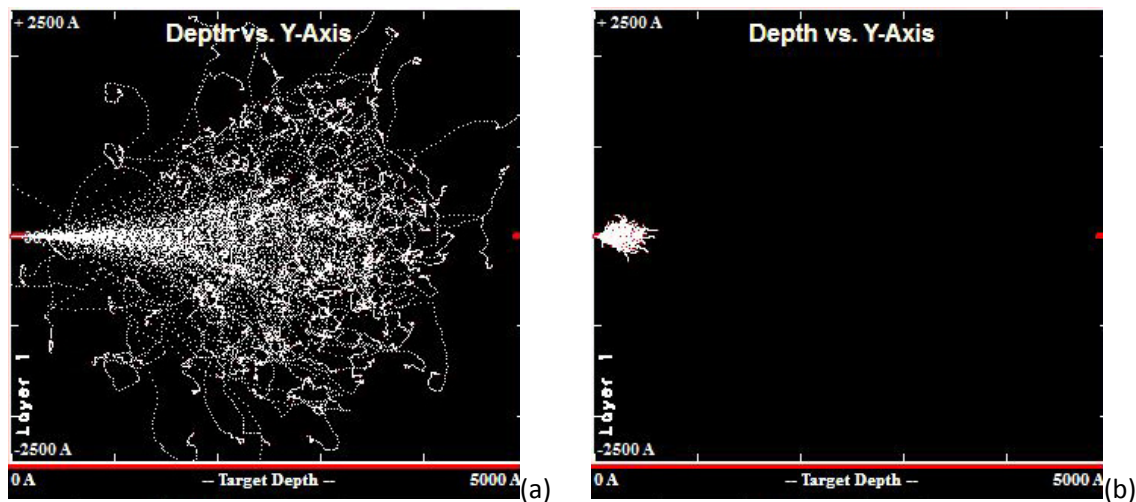

Figure 3: SRIM simulations of, (a) 30 keV He$^+$ ions into silicon (b) 30 keV Ga$^+$ ions into silicon. X and Y axis in Å.

From the simulations in figure 3, we can see the lighter He$^+$ ion with its greater velocity travels significantly further in silicon figure 3(a). Due to the many scattering events that the ions undergo, a large pear-shaped interaction volume to a depth of ~500 nm is evident, as well as

high angle lateral scattering extending perpendicularly to the beam's impact direction. Comparing to the Ga$^+$ interaction volume, in Figure 3(b), we see the entire ion dose is terminated close to the impact site, with the total penetration depth approaching ~50 nm. Furthermore, lateral scattering is also localised to ± 25 nm. Although the pear-shaped interaction volume is still evident, it is localised close to the surface in comparison with that of He$^+$ ions, even though the acceleration voltage is the same in both cases. This is due to the velocity difference between the ion species.

We can calculate the velocity of ions using eq. 5a below;

$$V = \sqrt{2eE/M} \qquad\qquad eq.\,5a$$

Where V is velocity, E is accelerating voltage, M is mass and e is the electronic charge.

If we take a Ga$^+$ ion and calculate its velocity at 30 kV using eq. 5a [14]-p16, we can then apply eq. 5b below to calculate the acceleration potential required to obtain the same velocity with different ionic masses:

$$E = \frac{MV^2}{e} \qquad\qquad eq.\,5b$$

We now have a method to directly compare the interaction of different ion species normalised with respect to their velocity. Also when the velocity is nomalised using the accelerating voltage we see the mass/charge ratio is now equal for the different ion species.
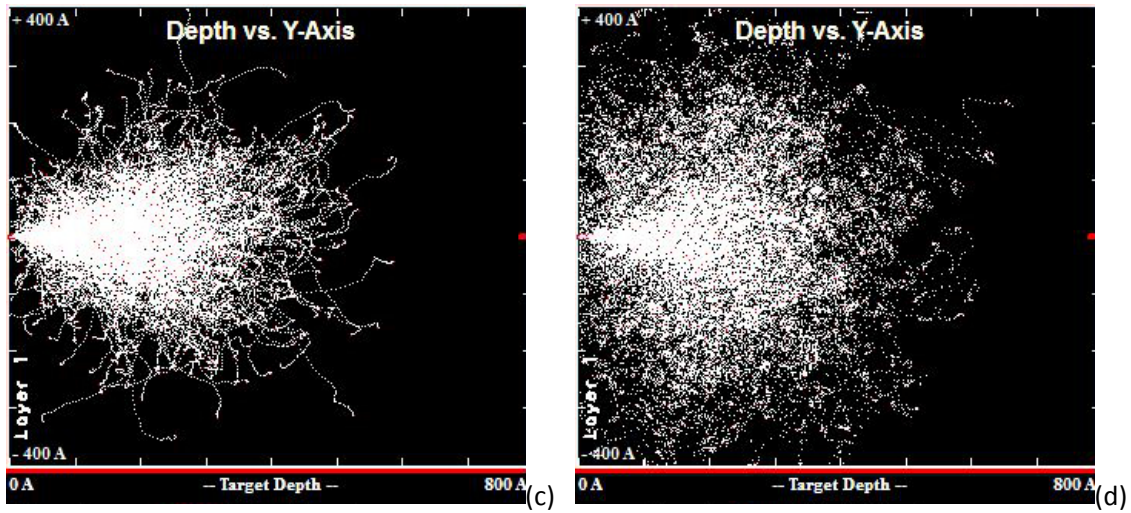

(a) (b)

9

(c)   (d)
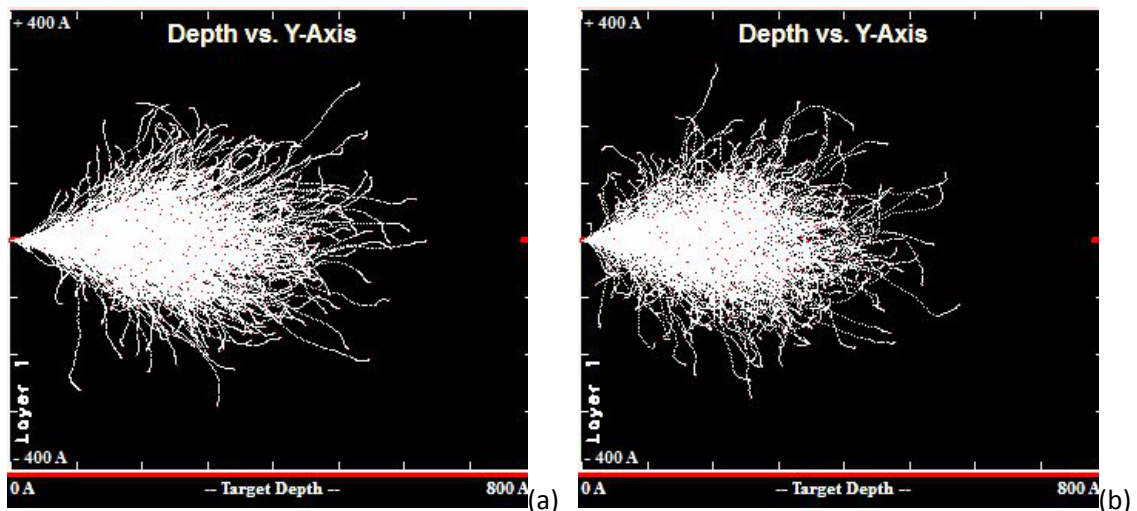
Figure 4: SRIM simulations of (a) 30 kV Ga$^+$ ions in Si, (b) 17 kV Ar$^+$ ions in Si, (c) 8.6 kV Ne$^+$ ions in Si and (d) 1.7 kV He$^+$ ion in Si. X and Y axis in Å.

As can be observed in figure 4 (a-d), controlling the velocities by adjusting the accelerating voltages brings stopping distance of the ions to approximately the same penetration depth.

The penetration depth of the ions, R, can be calculated using the Kanaya–Okayama expression. [15]-p18

$$R = \frac{kE^p}{\rho} \qquad\qquad eq.\,6$$

Where E is the beam energy in keV, ρ is the target material density p and k are constants where k is dependent on the particle type. Values for k and p are given in Table 1 below.

Table 1: Values k and p for the Kanaya-Okayama penetration depth model

Ion	k (nm)	p
Ga$^+$	8	0.72
Ar$^+$	10	0.72
Ne$^+$	16	0.72
He$^+$	80	0.72

Using eq. 6 the penetration depth as a function of acceleration potential can be calculated for a range of different ions. Figure 5 shows the ion penetration depth for helium, gallium, argon and neon species. Helium ions, red curve, penetrate deep into the surface at relatively low voltages. At 2.5 kV, the penetration depth already approaches 80 nm for He^+ ions. Comparing this to the heavier ions - neon, argon and gallium (green, blue and yellow, respectively) - the penetration depths progressively shorten as the ion mass increases. 30 kV Ga^+ ions have approximately half the penetration depth of He^+ ions at 2.5 kV.
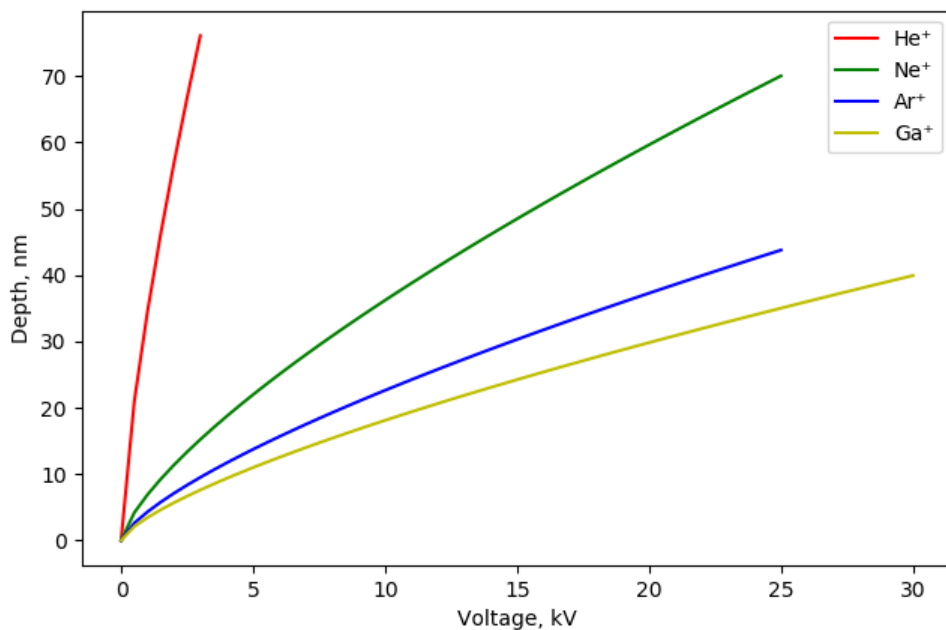

Figure 5: Plot of the penetration depths of different ionic species as a function of accelerating voltage

Table 2 displays the effect of adjusting the voltages. The penetration depth of the ion travelling into the bulk of the sample is known as the stopping range. The stopping range for a voltage is effected by straggle, ion straggle occurs as the ion goes through multiple collisions in the bulk, this creates the large interaction volume. Also if the ion experiences many collisions nearer the surface it will not travel as far into the bulk. The material the ion interacts with also affects the penetration depth, the heavier the element the greater the stopping power or shorter the penetration depth.

Table 2: Table of stopping ranges for Ga⁺, Ar⁺, Ne⁺, and He⁺ ions in Si with controlled voltages, and compared with all at 30 kV. The Kanaya–Okayama equation is a good approximation of the stopping distance while the SRIM software uses additional parameters improving the accuracy. Both values are displayed in the table.

Ion	Stopping range Using Kanaya–Okayama equation	Stopping range From SRIM software	30kV stopping range
Ga⁺ 30kV	39.9nm	28nm	39.9nm
Ar⁺ 17kV	33.1nm	23nm	49.9nm
Ne⁺ 8.6kV	32.5nmn	22nm	79.8nm
He⁺ 1.7kV	50.5nm	22nm	399nm

Adjusting the accelerating voltage also has an effect on the sputter yield, i.e. the number of atoms removed per incident ion. In most cases, reducing the accelerating voltage lowers the sputter yield, reducing the efficiency when thinning samples. The sputter yield from an ion-target collision can be calculated from eq.7 [16]:

$$Y = 0.042 \frac{Q\alpha^*(M_2/M_1)}{U_s} \times \frac{S_n(E)}{1 + \Gamma k_e \epsilon^{0.3}} \times \left[1 - \sqrt{\frac{E_{th}}{E}}\right]^s \qquad eq.7$$

Equation eq. 7 calculates the sputter yield based on target material, ion species and accelerating voltage, where M_1 is the mass of the accelerated particle and M_2 is the mass of the target atom, E is the energy of the accelerated particle in eV, $S_n(E)$ is the nuclear stopping cross section, k_e is the Lindhard stopping coefficient, ϵ the reduced energy expression, E_{th} is the threshold energy for the combination of ion and target, U_s is the surface binding energy of the target, Γ is a numerical factor and Q, α^* and s are fitting parameters.

As a result of mass differences, different ion species have varying sputter yields. Sputter yield also depends on the target material and the acceleration voltage of the ion.

Using eq. 7, the sputter yield for silicon at an acceleration voltage of 30keV can be calculated for each of our ion species; $He^+ = 0.02$, $Ne^+ = 0.87$, $Ar^+ = 1.6$ and $Ga^+ = 2.04$. For example, in the case of Ga^+ this essentially means that for each ion impact 2 atoms of Si are removed, whereas for He^+ 100 ions would be required to remove two silicon atoms. It is clear that the heavier ions are much more efficient at removing material.

Naturally, for the same impact ion, different target materials will have varying sputter yields. Also, the crystal orientation within a material can greatly affect sputter yields; this is due to channelling. Channelling is where the ion can travel in between atomic planes with little interaction. This preferentially reduces the sputter yield for that crystal direction resulting in different milling rates from grain to grain. Figure 6 shows preferential milling causing excessive changes to the surface topography. The effect has some advantages and can be used for imaging, as changing crystal orientations will have different secondary electron yields allowing for the direct imaging of grains on the surface of the sample. Figure 7 shows channelling contrast of copper grains.
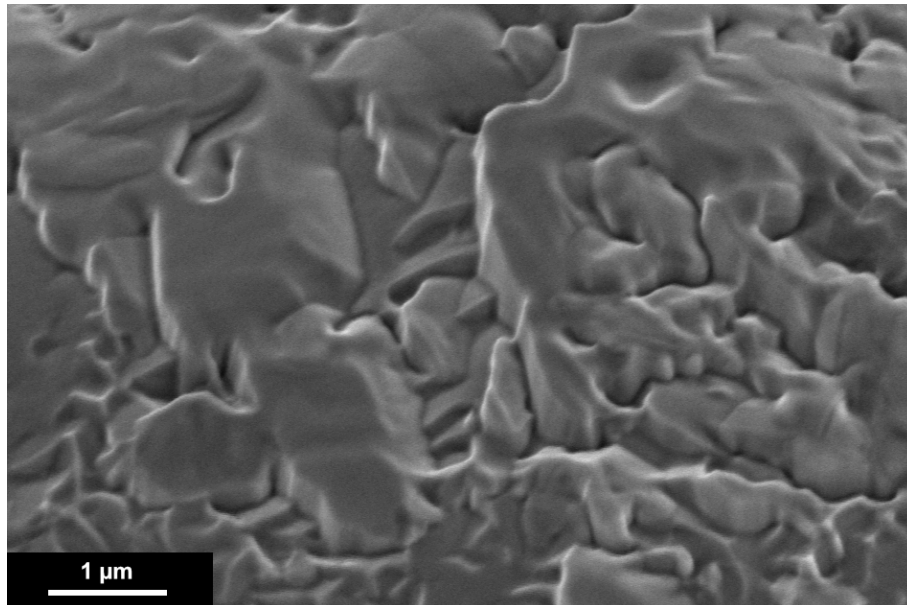

Figure 6: SEM image of the surface topography created on copper by preferential sputtering from a 30kV Ga^+ ion beam.
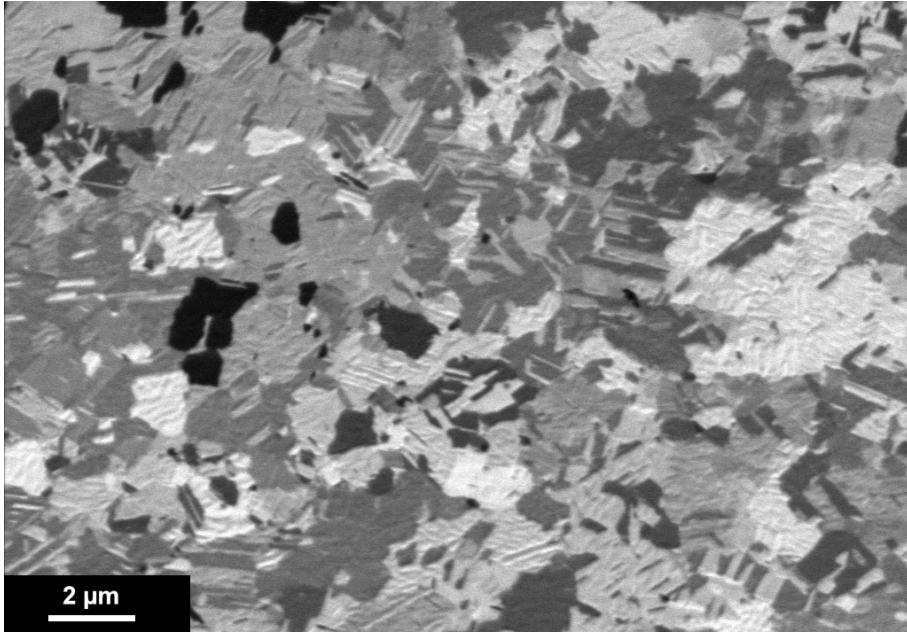
Figure 7: An example of ion channelling from copper grains imaging with a 30kV Ga$^+$ ion beam

Understanding electron and ion beam interaction theory is a pivotal aspect to successfully preparing specimens for characterisation, as well as enabling us to develop new techniques and technical approaches to sample fabrication. In the next chapter, the experimental instrumentation and approaches will be outlined.

4 Instrumentation

4.1 Electron source

The most common type of electron source operates by the principle of thermionic emission. This can be a thin tungsten wire bent to a fine point or a lanthanum hexaboride (LaB6) crystal. These sources are heated to high temperatures to emit electrons. Both types of tips have a cap close to them with a biasing voltage to draw off the electrons. The advantage of the LaB6 tip over the tungsten hairpin filament is the crystal is produced with a fine point giving better coherence and higher current density in a small probe.

Another type of source is the field emission [17] gun, FEG. There are two types of FEG the cold FEG and Schottky FEG. The Schottky FEG has a sharp tungsten tip normally coated in zirconia which is heated, so is a thermally assisted FE. The sharp point of the tip sits just outside a suppressor plate just below that sits an extractor. In both FE guns directly after the extractor, the electrons are accelerated to high voltage. A cold FEG uses a single crystal tungsten tip with an extremely fine point, this is held at a negative potential near an electrostatic extractor plate. The extractor is held at a high enough potential to extract electrons. When the electrons leave the tip they enter the accelerator and are accelerated to high voltage then fired down the column

In electron microscopes, the electron source, or gun, can dictate the ultimate performance of a microscope. The advantage of the cold FEG over the Schottky FEG is a reduced energy spread whilst this only gives a slight improvement in image quality (chromatic aberration) it can give massive gains in spectral resolution when performing analysis.

4.2 Ion Source

The ion source commonly used in a FIB microscope is the Ga liquid metal ion source (LMIS). The source has a tungsten needle and a reservoir of Ga, when the Ga is heated it flows down the needle to the tip where surface tension and high electric fields are used to form what is known as a Taylor cone. A large electric field is applied near the fine tip, this ionizes and extracts the ion through the field emission process [17].

He / Ne ion; Gas field ion source, the GFIS uses a fine point made up with just three atoms, a trimer. The trimer is produced from single-crystal 111 tungsten. A large electric field is applied at the tip of the three-atom trimer this is used to pull an electron from an atom of gas creating a positive ion. After the atom is ionised it is quickly accelerated away towards the extractor then into the probe forming optics down the column.

The GFIS source has a very low energy spread and can produce extremely small probes due to the fact the ions are produced in such a small area. One problem with the GFIS is it generates low current probes whereas the LMIS can produce probes with a large current making the LMIS source more suitable for milling and micromachining.

4.3 Lenses

In order to use a beam of charged particles for microscopy, we have to be able to focus the beam as we would with an optical light microscope. In 1926 Bush developed the first electromagnetic lens with the ability to focus electrons, conceptually similar to focussing light with a glass lens. This led the way for charged particle microscopes.

The concept of the electromagnetic lens is simple: if current is passed through a wire, the moving electrons generate a magnetic field; as the number of electrons travelling along the wire is increased, (the current) the magnetic field is increased. Eq. 8 [18]-p137 shows the relationship between the magnetic field and current load for a linear conductor.

$$B = \frac{\mu I}{2\pi r} \qquad\qquad eq.\,8$$

Where B is Field in Tesla, μ is Permeability (air or Vac 1.256^{-6}), I is Current in Amps. The $2\pi r$ term is a geometric factor.

Now, if the wire is wound into a coil the field can be increased furthermore, and again, by increasing and decreasing the current flowing through the wire, the strength of the magnetic field can be changed. This allows a beam of electrons to be focused. Eq. 9 [19]-p137 shows the relationship between the magnetic field and current for a conductive coil.

$$B = \frac{\mu NI}{L} \qquad\qquad eq.\,9$$

Where B is Field in Tesla, μ is Permeability (air or Vac 1.256^{-6}), N is the Number of turns, I is Current in Amps and L is Length of wire in meters.

The reason electrons can be focused by magnets is because moving electrons (and charged particles generally) have their own magnetic moment, hence a magnetic field can exert a force on the electron. As we can see in eq. 10 [19]-p123, using magnetic fields is particularly useful to focusing/controlling high-speed electrons. As the electron's velocity increases, its angular momentum increases, and in turn has a larger magnetic dipole moment and, therefore, the greater the effect of the magnetic field in the lens.

$$\mathbf{F} = e(v \times B) \qquad\qquad eq.\,10$$

Where e is charge of the electron, v is the Speed of the electron and B is Field in Tesla. This equation describes the force acting upon an electron in a magnetic field.

If we now consider ions, the issue with focusing Ions is that they have an enormous mass compared to electrons. For example, a Ga^+ ion would require a magnetic field 360x stronger than an electron. For this reason, electrostatic lenses are instead used for Ions. These lenses are basically charged plates that generate an electric field; the electric field in turn, applies an accelerating force on the charged particle:

$$\mathbf{F} = eE \qquad\qquad eq.\,11$$

Where e is charge of the electron, E is the electric field in volts.

The advantage of using electrostatic lenses is that the force acting on a charged particle is the same for Ga^+ as an electron; and the fact the ion is a lot heavier than the electron means it has a much lower velocity, resulting in the ion spending more time in the field with force acting upon it. The disadvantage of using electrostatic lenses is that when the charged particle is travelling at high velocity, it is only in the field for a short period of time; this means that to focus high voltage, fast-moving electrons, very high lens voltages or long lenses are required.

Figure 8 displays the force of an electric field and a magnetic field on an electron at increasing accelerating voltages. As we can see the magnetic field's force on the electron increases as the accelerating voltage and velocity increase.
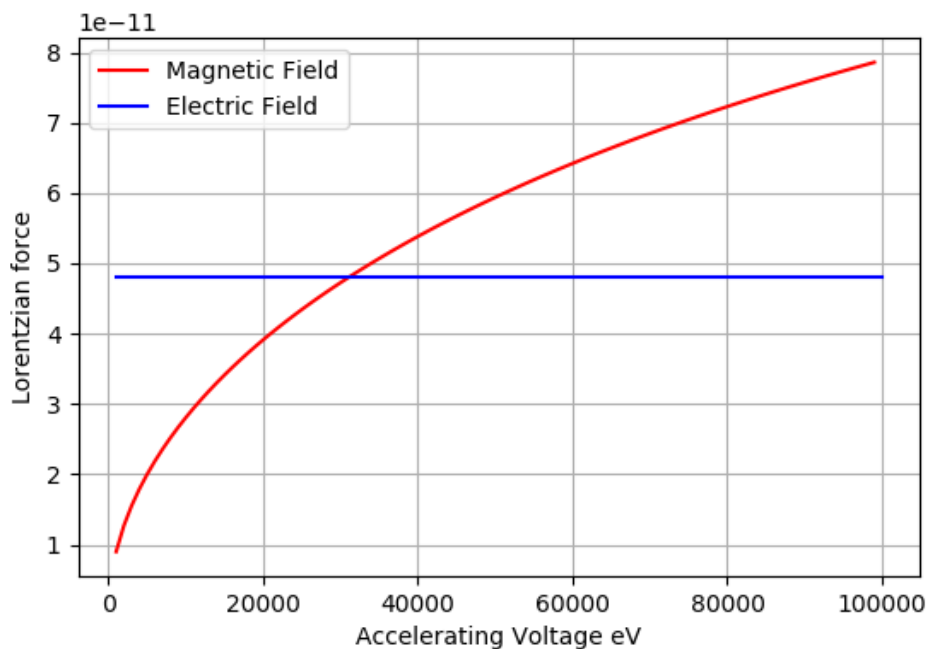

Figure 8: Graph displaying Lorentzian force acting on an electron at increasing accelerating voltage, in a magnetic field – red, and an electric field - blue

Most microscopy techniques, whether it is light, electrons or ions, have a similar lens configuration. As can be seen in figure 9, the optical and electron microscopes have a source then the first lenses the beam passes through are the condenser lenses. These lenses are the probe forming optics. They shape the probe that interacts with the sample, whether that is a parallel beam of electrons or a convergent probe. The beam will also pass through at least one multipole lens, which is used for removing distortions introduced by the non-perfectly-round lenses. After the beam is formed, this is focused onto the sample by the objective lens. For transmission electron microscopes there are a series of projector lenses after the objective lens. These lenses transfer relevant signals to imaging devices, detectors and spectrometers.
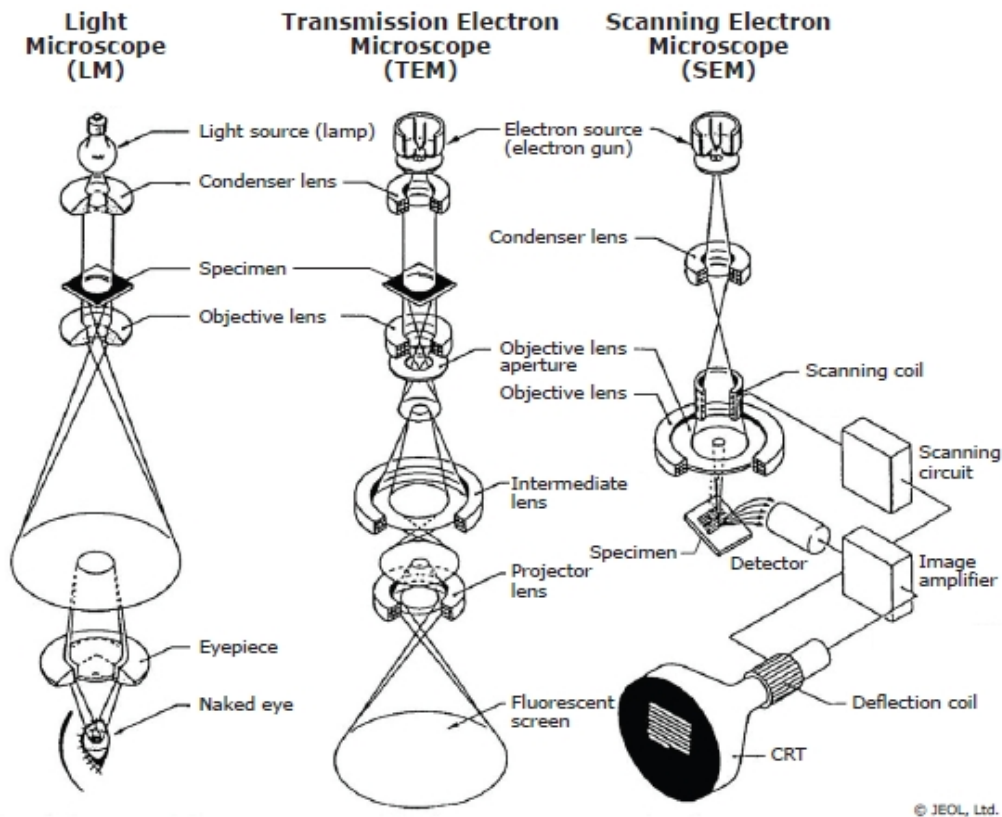
Figure 9: The image above displays the similarities in the lens configuration for different microscopy techniques [20]

4.4 Instruments

Throughout this thesis, we apply several techniques for specimen analysis, fabrication and preparation. We will firstly outline the electron microscopy techniques used during this work. We then move on to outline the Ion beam instrumentation. For clarity, electron and Ion beam sources and lenses are described. More in-depth descriptions go beyond the scope of this thesis and can be found elsewhere. [9] [21] [22]

4.4.1 Scanning/Transmission electron microscope: S/TEM

A Transmission Electron Microscope (TEM), or conventional TEM (CTEM) uses a parallel beam of electrons that are accelerated towards and pass through the sample. The electrons interact with the atomic structure of the sample, this enables high-resolution images to be produced. Magnification is produced by interacting with small areas, the electrons that exit the specimen from the small area of interaction are then projected onto a phosphor screen, photographic

film or a CCD camera. Some TEM's can be aligned and used as a Scanning Transmission Electron Microscope (STEM). In a STEM the beam still passes through the sample but instead of a parallel beam of electrons, as in CTEM, it employs a convergent beam focused to a small probe. This fine probe is then scanned across the sample. The beam scanning smaller areas and being displayed on a CRT or computer screen produces magnification, with the resolution in STEM dictated by the size of the probe that can be produced. A big advantage of using STEM mode is the ability to perform highly localised analysis.

The S/TEM instrument used for this project is an FEI Titan operating at 300kV, this instrument uses an EDAX 30mm^2 Li drifted EDX detector and Gatan Tridium EELS spectrometer for analysis.

4.4.2   Scanning Electron microscope: SEM

The operation principle of SEM is similar to STEM, where a fine probe of electrons is scanned over small areas of the sample; the main difference is the SEM is designed to study the surface of bulk samples. When a beam of electrons hit the surface they generate secondary electrons, due to the low energy of the secondary electron it has a limited escape depth which allows detailed imaging of the surface to be performed. The SEM's used during this project are a Zeiss Supra 40 and the electron column on the Zeiss Auriga dual beam FIB. Both instruments use the Zeiss Gemini column and were operated at 5kV.

4.4.3   Focussed Ion beam microscope: FIB

The FIB is almost identical in operation to the SEM, however the FIB uses a beam of charged ions. Also, like the SEM, the FIB generates secondary electrons, useful for surface imaging. The drawback with using a FIB as an imaging instrument, is the damage that is caused by the ion interaction with the sample. Dual-beam systems, combining a FIB and SEM, can be advantageous for sample preparation as you can monitor progress in real time during ion beam fabrication; imaging with the electron beam while the ion beam removes material.

4.4.4 Multiple Ion Microscopy; NanoFab

The NanoFab is the second generation He^+ ion microscope from Zeiss, the NanoFab uses three different ion species He^+, Ne^+ and Ga^+. The main column in the system can switch between helium and neon gas, then there is a separate gallium FIB column. The motivation for developing the original He^+ ion microscope is to provide new alternative to the SEM. Developed by ALIS (Atomic Level Imaging Systems) who were bought out by Zeiss in 2007 with the first production instruments being delivered in 2008. Why use He^+? The He^+ ions give very surface-sensitive imaging, when the He^+ ion interacts with the sample surface, secondary electrons are produced. He^+ ions do not suffer from backscattering effects like electrons do so the signals are generated where the primary beam interacts without spreading giving a very localised imaging . The fast-moving ions do penetrate into the sample's bulk and generate secondary electrons; however their low energy means that they cannot escape to the surface. Light ions also do not damage the surface as much as heavy ions do. Another advantage of using the He^+ ion microscope is that the optics create a parallel probe or probe with very low divergence; this gives a huge depth of field compared to SEM. The source design allows extremely small probes to be produced. Also having greater mass than an electron, the He^+ ion De Broglie wavelength is very short, for example a 30keV electron has a wavelenght of 7pm while a 30keV He^+ is 0.080pm, meaning that diffraction limit will not be a problem. This highly localised, surface-sensitive imaging, combined with large depth of field, makes for a very exciting imaging instrument. In addition to all this, the He^+ ion microscope holds one extra trick up its sleeve: because it uses ions, an electron flood gun can be used to neutralise charge from non-conducting samples. This means that a sample coating is not required. Although the He-ion microscope is a very powerful imaging instrument for the scope of this project we are solely interested in whether it is possible to utilise the low-mass ion interactions for localised gentle sample preparation. Ne^+ ions have similar characteristics to He^+ ions, but are slightly heavier and give a higher sputter yield making them more suited to nano scale fabrication. The Ga^+ FIB column would be used for bulk cutting.

4.4.5 Argon Ion milling; NanoMill

The instrument used for the final thinning and polishing of the samples is a Fischione NanoMill. The main reason this instrument is used is because it works at low voltage 50V – 2kV and uses relatively light argon ions. The NanoMill uses an impact source to generate ions, the impact source works by bombarding the Argon gas with electrons when the gas is ionized creating an

Ar$^+$ ion it is attracted to the extractor plate, accelerated and focused on the target material. The simple design of the impact source is relatively low maintenance and allows large probes with high beam currents to be produced, but would not be suited to high resolution applications

An argon ion polisher has been the standard for post-polishing mechanically thinned and FIB samples for many years now. A traditional broad ion beam (BIB) polishing system would have a beam diameter of around 300 microns. Generally, these systems use a static beam: the sample is placed under the beam and rotated, which is fine if you have a large-area like a mechanically thinned sample; however, if you have small 10-micron-wide lamella on a grid, then the beam would be interacting more with grid and sample-holder, rather than the sample itself. The NanoMill has an advantage over these classical broad beam systems as it uses a new design of ion gun that allows smaller beams to be formed and gives a localised interaction of the ion beam with the sample. The localised interaction reduces milling of the support grid and the consequent redeposition of grid material on to the surface of the sample.

Beyond imaging, we can utilise the secondary signals produced when a high energy charged beam interacts with a sample. In the next section we discuss spectroscopic and analytical techniques.

5   Analytical Techniques

5.1   Energy Dispersive X-ray (EDX) spectroscopy

As discussed in the electron theory section, an electron beam can generate signals useful for characterising materials. As we can see in figure 10, through inelastic interactions we can generate characteristic x-rays. The x-rays generated can be measured using an EDX detector. The EDX detector has a crystal that collects the x-rays emitted by the sample, the x-rays yield free electrons in the crystal, an electrical charge bias is produced (a range of voltages are produced). The voltage of the electrical pulse generated corresponds to the characteristic x-ray of the element.
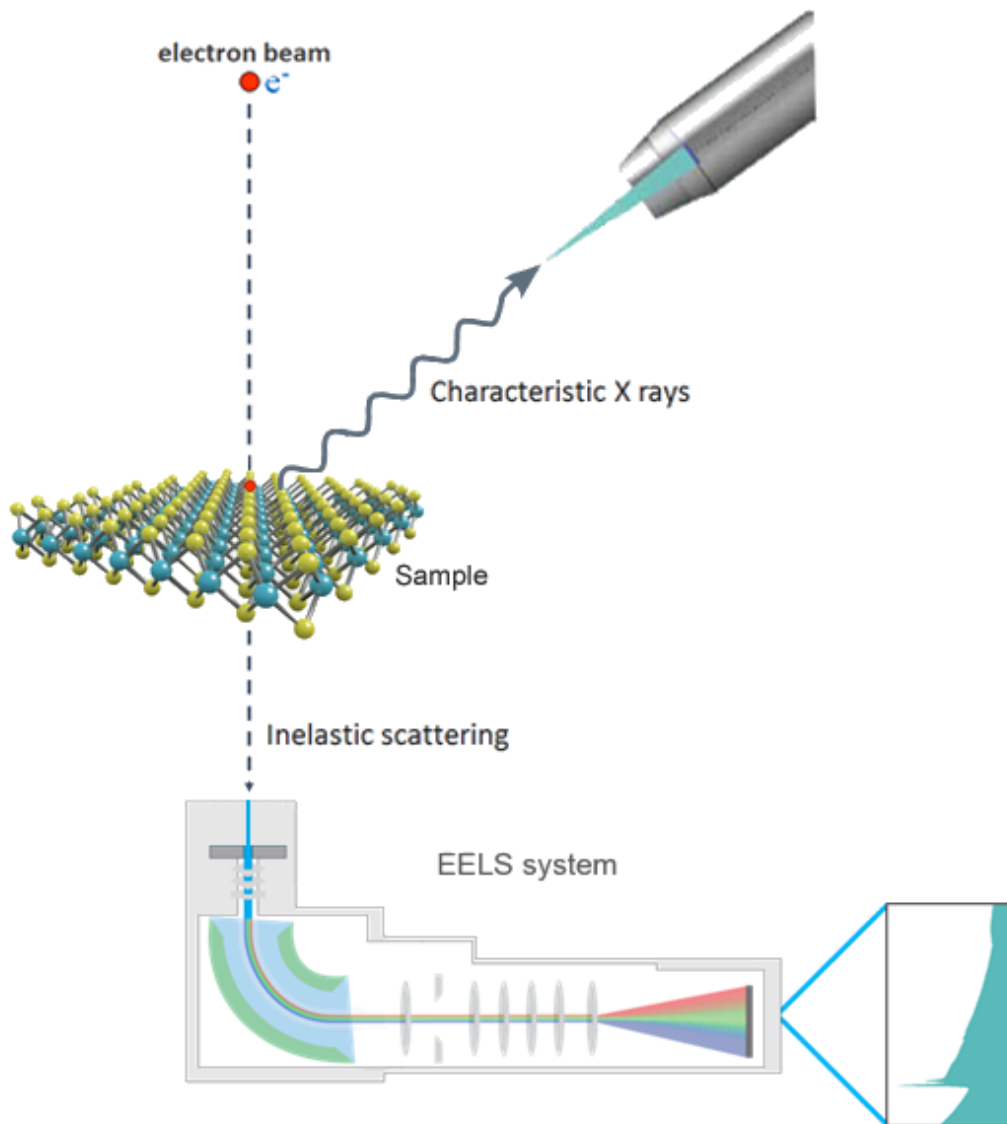
Figure 10: An electron interaction with sample producing signals for EDX and EELS analysis [23] [24].

5.2 Electron Energy Loss Spectroscopy (EELS)

Figure 10 shows an incoming electron interaction with a core shell electron, as discussed above this interaction generates an x-ray. Another consequence of this interaction is the incoming electron loses energy, this energy loss can be measured using an EELS spectrometer. The EELS spectrometer uses magnetic lens that deflects these electrons through a 90° angle. This effectively acts like a magnetic prism, separating out the different kinetic energies from the electron beam that has passed through the sample. The transfer optics combined with slits allow a range of kinetic energies to be imaged on a CCD detector. A profile of this image displays intensities at different energies, this spectrum indicates what elements the beam has interacted with as it has passed through the sample.

5.3 Image analysis

Imaging software is a key component to the post-processing of acquired microscopy data. The image analysis software, when given a correctly calibrated image, allows quick and simple point to point measurements to be made and adjustments to contrast and brightness. Some software packages come with a comprehensive suite of tools and can perform tasks such as particle sizing. One tool that is often used when analysing TEM images is the Fast Fourier Transform, FFT. An FFT is a mathematical algorithm which converts a signal from its original space domain to a representation in the frequency domain. This means periodic features appear as spots in the FFT. Figure 11 A and B are examples of how a series of evenly spaced lines appear as two spots in the FFT. Generating an FFT from an image or a region of interest within an image can help to accurately measure a lattice spacing in a TEM image.
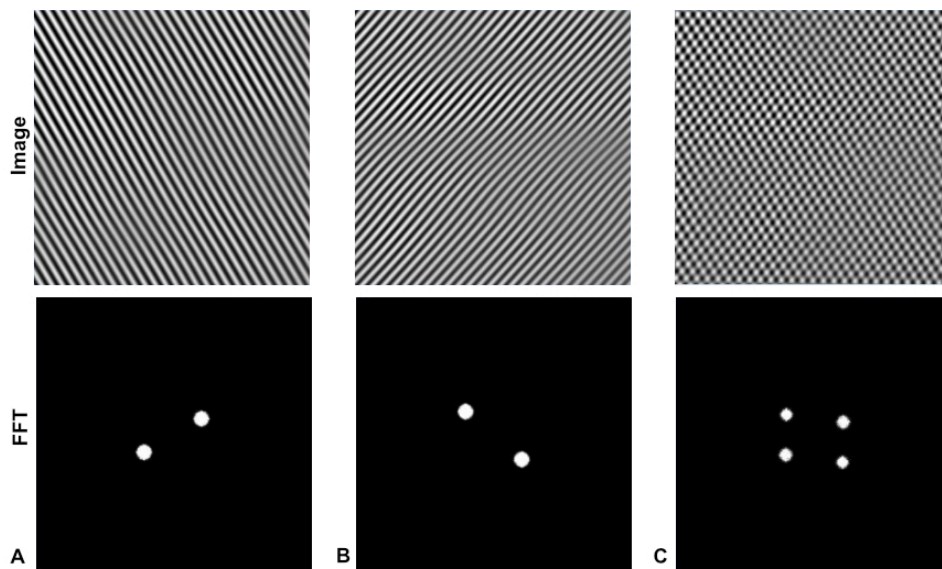
Figure 11: A-C images of periodic features with accompanying FFTs below

6 Experimental chapter: Ion Species Experimental Investigation

6.1 Experimental Overview

The primary aim of this investigation is to study the suitability of commercially available light ion instruments for improving sample preparation for high-resolution electron microscopy. The Zeiss NanoFab, for example, has a He^+ and Ne^+ GFIS source, as well as a separate Ga^+ LMIS column, which gives the potential for complete sample preparation *in-situ* without the need for post-processing.

He^+ ion and Ne^+ ion microscopy is a relatively new technique and there is still a lot more to understand about their materials interaction. The current literature is conflicting on the subject of milling bulk samples using He^+ and Ne^+ ion beams. For example, it has been claimed that He^+ ions can be used to improve the quality of a silicon lamella [25]. Also a combination of Ga^+ and Ne^+ polishing using the ZEISS NanoFab could be used to produce samples free from Ga^+ and amorphous layers while maintaining the good crystallinity [26]. In contrast, it has been claimed that a He^+ ion beam does not show any appreciable sputtering and an increase in the dose only introduces further ion implantation and more subsurface damage [27]. Also, when He^+ and Ne^+ ion beam etching have been investigated, subsurface damage and bubbling was observed with both ion species [28].

In this study, the Zeiss Nanofab is utilised to observe and understand the interaction/damage mechanism of different light ion species interaction with a silicon sample. This was achieved by implanting the selected ion species into the top surface of a ~1µm thick silicon lamella. The lamellae were then thinned with low voltage Ar^+ until electron transparent and imaged using TEM. Low voltage Ar^+ was used to prevent any additional damage, and to preserve the specimens state after interaction with the ion species under investigation. The ion species under investigation during this project work were neon (Ne), helium (He) and gallium (Ga). These were investigated at similar doses and analysed in TEM.

6.2   Materials and Methods

Throughout this study prefabricated single-crystal Si lamellae, manufactured via the Bosch process, are used (purchased from Kleindiek Nanotechnik GmbH). The Bosch process uses a gas such as SF_6 and a strong oscillating electric field to produce a plasma of reactive ions, the reactive ions etch the target surface and can produce high aspect ratio features in the silicon [29]. As can be seen from figure 11 and 12, the Bosch process is used to produce an array of silicon lamella attached to a central support bar on one side. The array of prefabricated, highly uniform Si lamella is extremely useful for several reasons; firstly, for efficiency. Manufacturing could be in fact optimised, not needing to go through bulk preparation. Bulk milling using a FIB can take several hours depending on the material beam current and sample size required. Secondly, as the lamellae are prefabricated to a uniform thickness, further thinning can be performed using argon (Ar) ion milling below 1kV. Ar^+ ion milling is extremely important as it minimises potential heavy-ion artefacts from a Ga FIB such as lattice disruption and amorphisation. Furthermore, the Bosch process provides uniformity and consistency across the array of lamellae, which is difficult to obtain with conventional FIB sample preparation.

6.2.1   Lamella Preparation Method

The Bosch processed lamellae were loaded into a Zeiss Auriga dual-beam FIB/SEM, where a standard lift-out procedure was performed [3] [22]-p213. This standard lift-out technique consists of several steps allowing us to isolate an individual lamella to perform further experimentation on. The experimental setup is shown in figure 12. A nanomanipulation needle is driven close to the selected Si lamella. The nano-manipulator is highly controllable multi-axis manipulation device, with ~10nm stepper control. The nano-manipulator utilises a fine tungsten whisker attached to the end of the needle. This can be seen in figure 12. The whisker is extremely delicate with a ~100nm tip apex.

In order to attach the needle to the selected lamella, we use a Pt gas injection system (GIS). The GIS Flows Pt gas that reacts under the beam, enabling either electron beam induced deposition (EBID) or ion beam induced deposition (IBID). This can be used to deposit protective layers or weld the manipulator to the lamella. The Pt GIS needle is one of four GIS needles, shown in the upper part of figure 12. The Pt GIS needle is driven to a position just above the lamella.
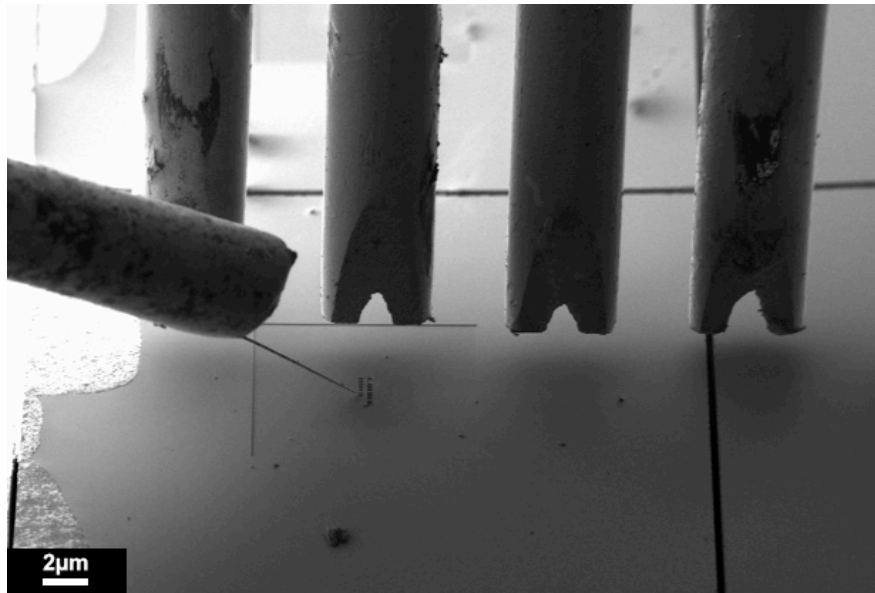
Figure 12: The nano manipulator in position to be attached to the prefabricated Si lamella with the gas injectors above.

Once the manipulator needle and Pt GIS are positioned close to the lamella, the manipulator needle is driven into contact with the upper left corner of the lamella. Figure 13 (a) shows the manipulator needle approaching the lamella. Gentle and controlled movements are extremely important here as the lamella structure is delicate and prone to mechanical damage during manipulation.
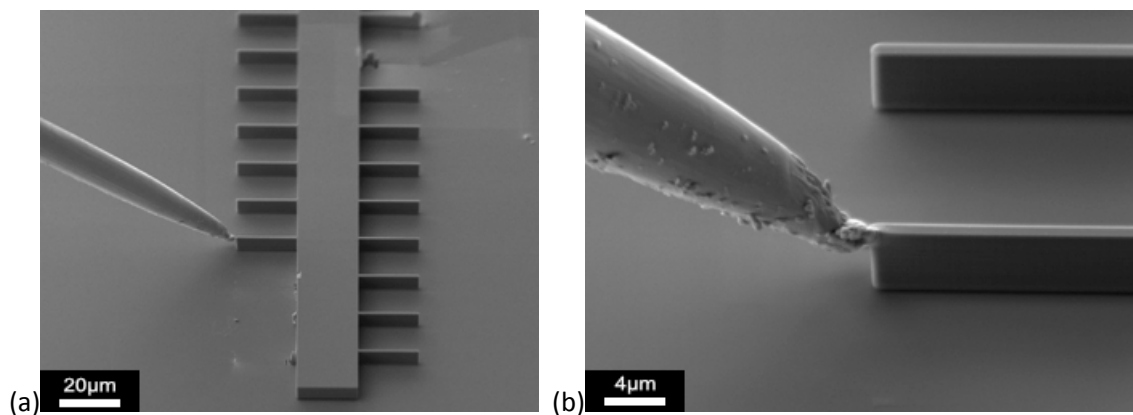

Figure 13: (a) The nano manipulator next to the array of lamellae **(b)** A Kleindiek nano manipulator was welded using platinum (Pt) electron beam-induced-deposition (EBID) to the Si lamella.

The needle is attached to the lamella via a localised Pt EBID 'weld'. Pt GIS needle directly above the lamella allows localised and controlled deposition enabled by electron beam irradiation of the area. As can be seen in figure 13 (b), the Pt deposition is localised to the needle-lamella contact point.

When the lamella is securely attached to the needle it can be safely removed from the support bar. This is achieved by using the Ga FIB to locally mill the connection point between the lamella and support bar. Figure 14 clearly shows the FIB cut at the junction, completely freeing the lamella from the substrate. The lamella is then lifted away from the substrate for further processing.
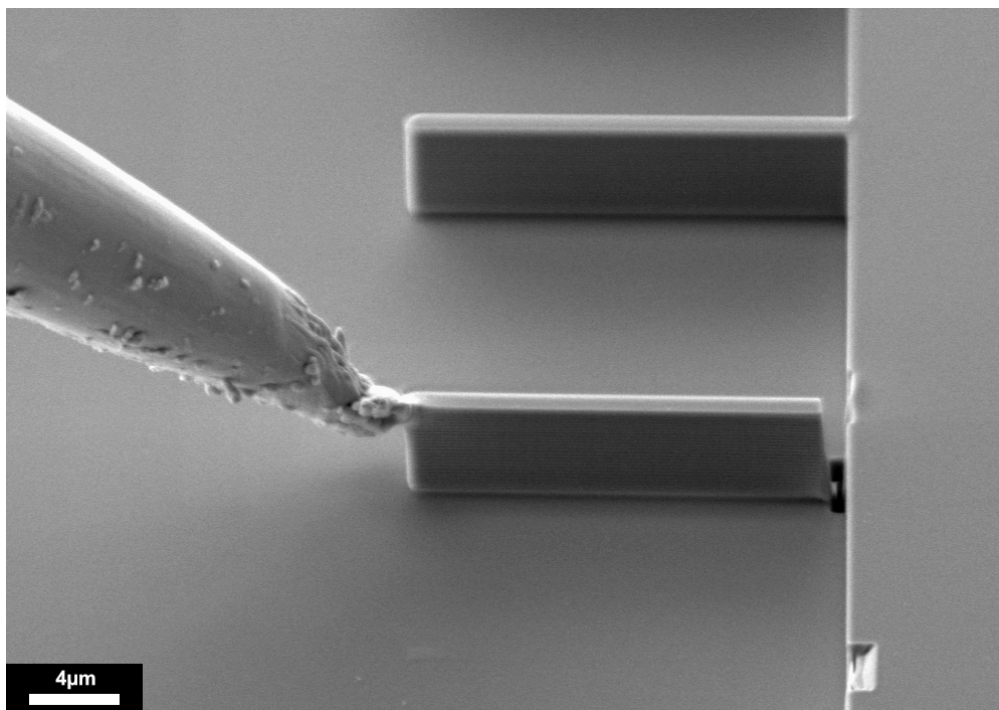
Figure 14: Following that, the supporting side was milled away using the Ga^+ ion beam.

The lamella can now be attached to an omniprobe TEM support grid. The omniprobe grid is a semi-circular 3mm diameter copper grid designed for lamella processing and TEM imaging. It consists of 3, or more, copper support legs that protrude from its flat side. The lamella is attached to one of the copper legs, allowing for sample thinning, top down ion implantation, and, cross-sectional imaging.
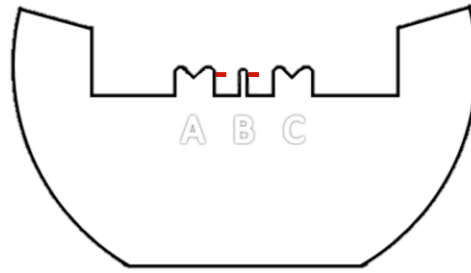
Figure 15: Omniprobe TEM grid, with lamella positions marked in red

The omniprobe grid is mounted vertically in the chamber, parallel to the normal axis of the lamellae surface. The lamella is attached to the omniprobe grid by driving the nano manipulator needle until the opposite side of the lamella is in contact with a grid leg, figure 16(a). It is important to place the lamella close to the top of the grid leg. The lamella is then attached to the grid via Pt-EBID, with the lamella cut away from the needle via FIB, clearly seen in figure 16(b).

(a)   (b)
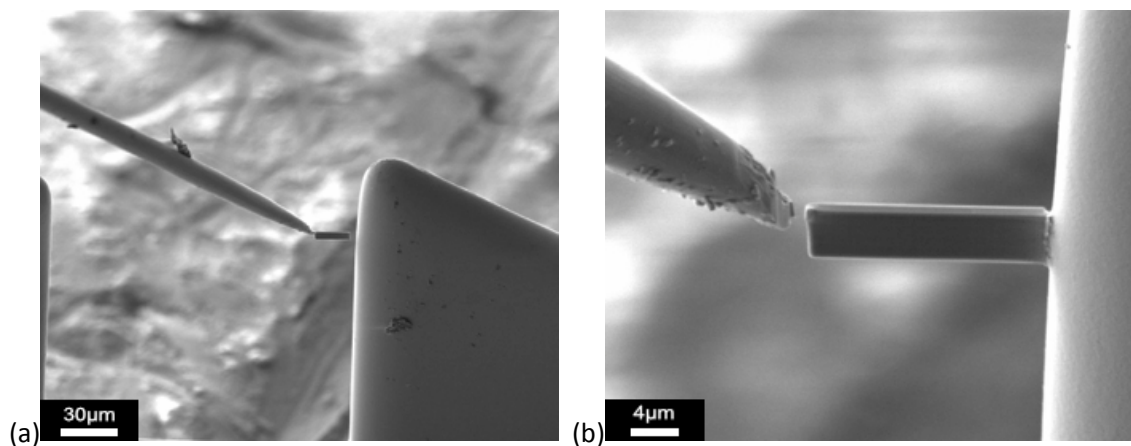
Figure 16: (a) The lamella was put in contact with copper post on the TEM grid (b) the lamella is EBID-Pt welded onto the post and the nano manipulator needle is cut away.

After the lamella is secured to the grid the sample is thinned to ~1µm using a 15kV Ga beam. This removes topographical features from the Bosch process. There are two reasons for leaving the sample thick; firstly the ion beams go through a bulk interaction if we refer back to figure 3a we can see that He$^+$ ions have a large interaction volume at 30kV due to the light ions scattering through the bulk. The light ions spread ~500nm laterally in the bulk, we want to capture the whole of this interaction. Secondly, the rest of the thinning process is completed

using low voltage argon (Ar^+). This is to reduce structural defects, such as lattice disruption and amorphisation, that can be introduced by more energetic beams.

After the lamellae are prepared, they are loaded into the relevant instrument for ion bombardment. The Ga^+ experiments were performed in a Zeiss Auriga, He^+ ion and Ne^+ ion experiments were performed in a Zeiss NanoFab. The geometry is the same for all the instruments where the beam is parked on the top surface with the stage at zero degrees tilt for a direct surface impact.

All of the thinning and final polishing was performed by Ar^+ ion milling in a Fischione NanoMill at low voltage, 900v. After the sample was sufficiently thinned S/TEM imaging and analysis was performed in an FEI Titan operating at 300kV. The samples are imaged in STEM mode, high-resolution images were acquired to investigate the effect of the different ion beams on the crystal structure.

6.3 Interaction of Ga$^+$ ions in silicon

In the first study, we investigate the interaction between Ga$^+$ ions and Si lamella. The Ga$^+$ FIB is the industry standard, and benchmark technique, for lamella preparation and can be used for complete sample preparation.

In this experiment, we firstly prepare a bulk lamella specimen using the procedure outlined the lamella preparation section. The lamella is mounted into A Zeiss Auriga, then the sample is orientated is so that the ion beam is incident on its top surface. This arrangement is evident in figure 16, which shows an SEM image of the lamella. We can clearly see two ion milled pits in the top surface of the lamella. Furthermore, figure 17 shows that our lamella preparation technique provides a large area to experiment, with ~15µm lamella length to work with.

To perform the experiment a focused probe of 30keV Ga$^+$ ions with a probe current of 20pA was positioned above the top surface of a lamella. The lamella is at zero degrees tilt relative to the ion beam. The selected area is exposed for 1.65 seconds, giving a total ion dosage of 2.06 x 10^8 ions, this works out to 7.3 x 10^{18} Ga$^+$ ions/cm^2, as calculated from eq. 12.

$$D = \frac{(I/e)\, t}{A} \qquad\qquad eq.\, 12$$

Where ion dose, D, is related to the beam current, I, in amps and time, t, is in seconds. e is the electron charge and A is the beam interaction area in cm^2. (Ion beam probe size was measured using the technique described in appendix 1)

Again from figure 17, we can clearly see the interaction area even at low doses, due to the large atomic mass of the Ga$^+$
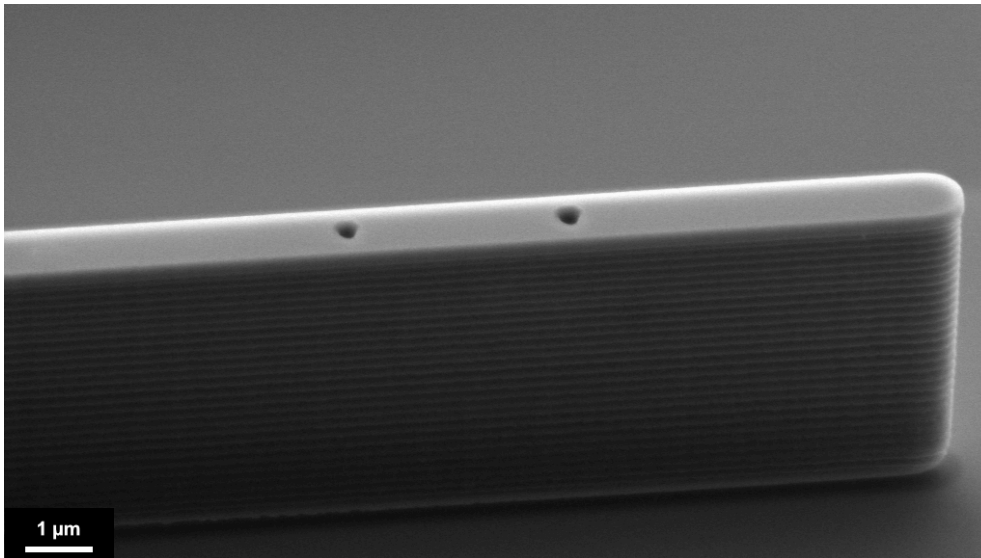
Figure 17: SEM image of Ga$^+$ beam interactions, it is clearly visible where the Ga ions have drilled little holes into the top surface of the Si.
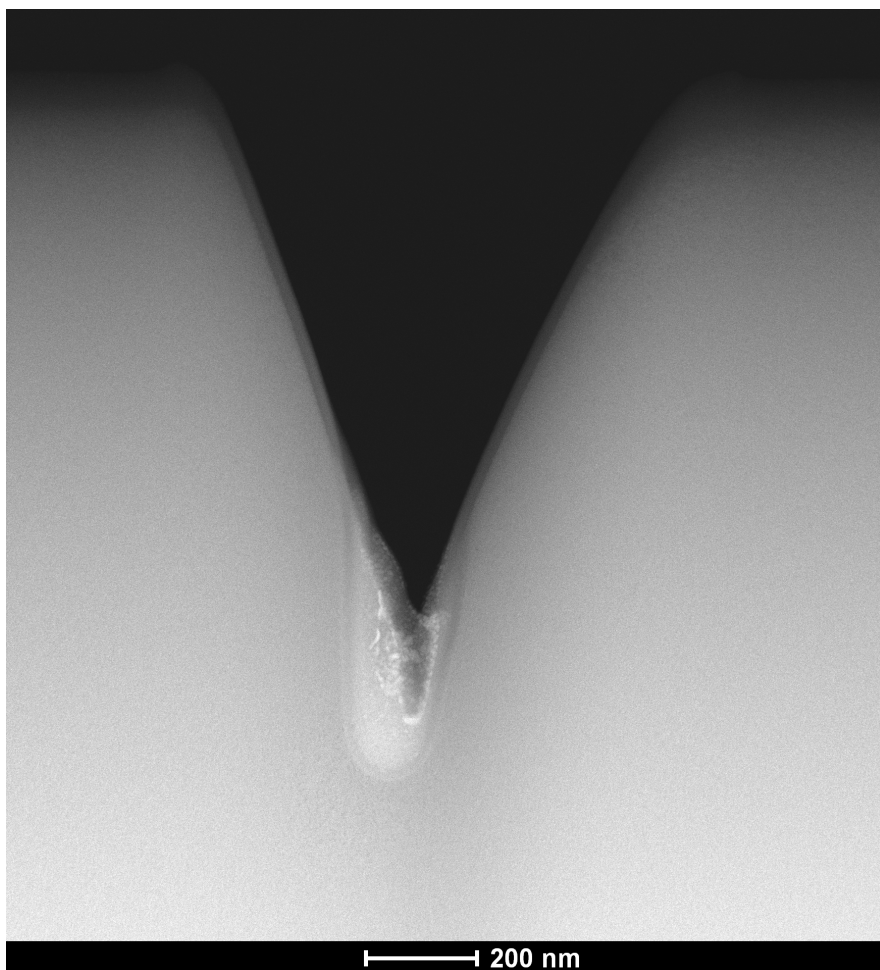
Figure 18: HAADF STEM image overview of Ga$^+$ interaction

The HAADF image in Figure 18 displays the cross-section of the Ga$^+$ ion interaction. This shows a neat V-shaped cut into Si. The interesting thing about this is not only how efficiently the Ga$^+$ ions have removed material but also how neat the sides of the cut were, as there was only a thin 20nm amorphous layer. At the bottom of the V, some of the negative effects of the Ga$^+$ beam can be observed. The brighter areas are where Ga has been implanted into the silicon. To verify the presence of Gallium in the sample EDX analysis was performed, the electron beam was scanned over a the area highlighted in red on figure 19(a), this is the bright area at the bottom of the cut, an EDX spectrum was collected clearly showing the presence of gallium figure 19(b).

(a)

(b)
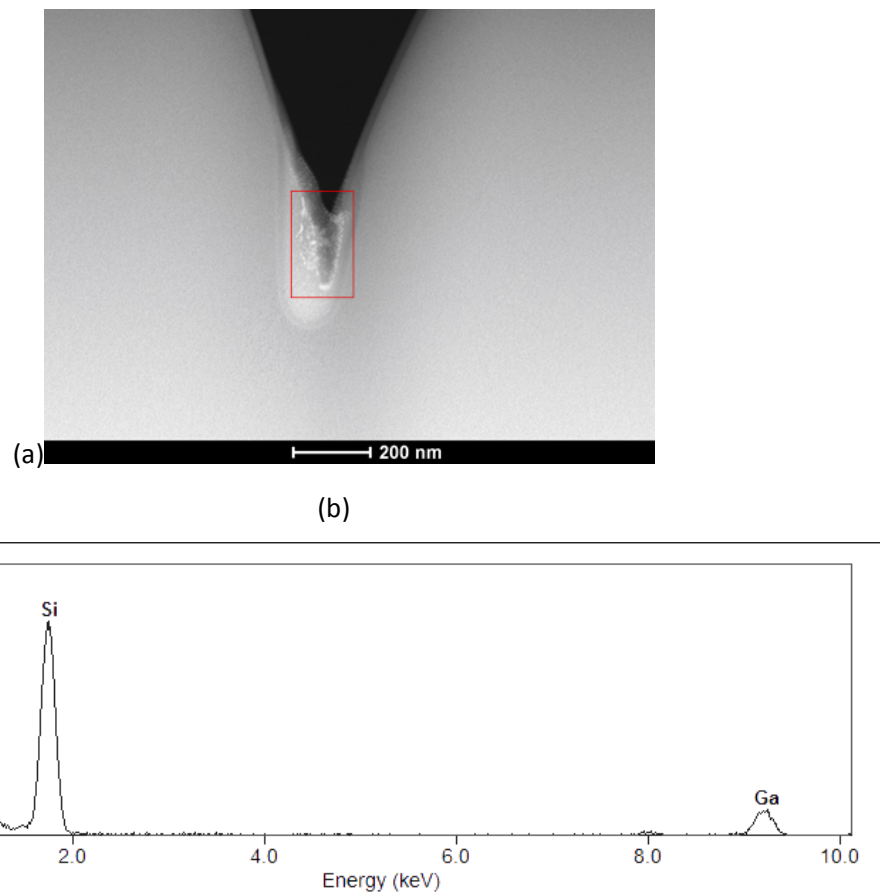
Figure 19: (a) STEM image showing Ga$^+$ ion V-cut red box marks the area analysed, (b) EDX spectroscopy from the area within the red box

Using EDX for elemental identification, you can clearly peaks at 1.1kV and 9.2kV showing that the brighter areas at the bottom of the pit are Ga$^+$ ions that have been implanted into the Silicon.

A closer look at the side walls shows a uniform amorphous layer ~20nm thick as can be seen in figure 20. Figure 21 is a high-resolution STEM image of the sidewall here we can see the amorphous region abruptly returns back to fully crystalline.
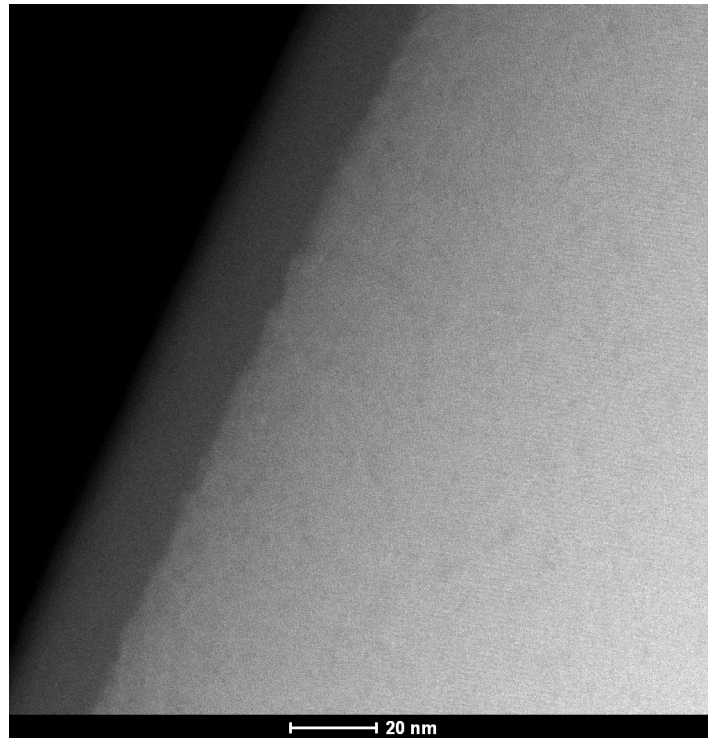
Figure 20: HAADF STEM image of Side of the Ga$^+$ ion cut into Si lamella
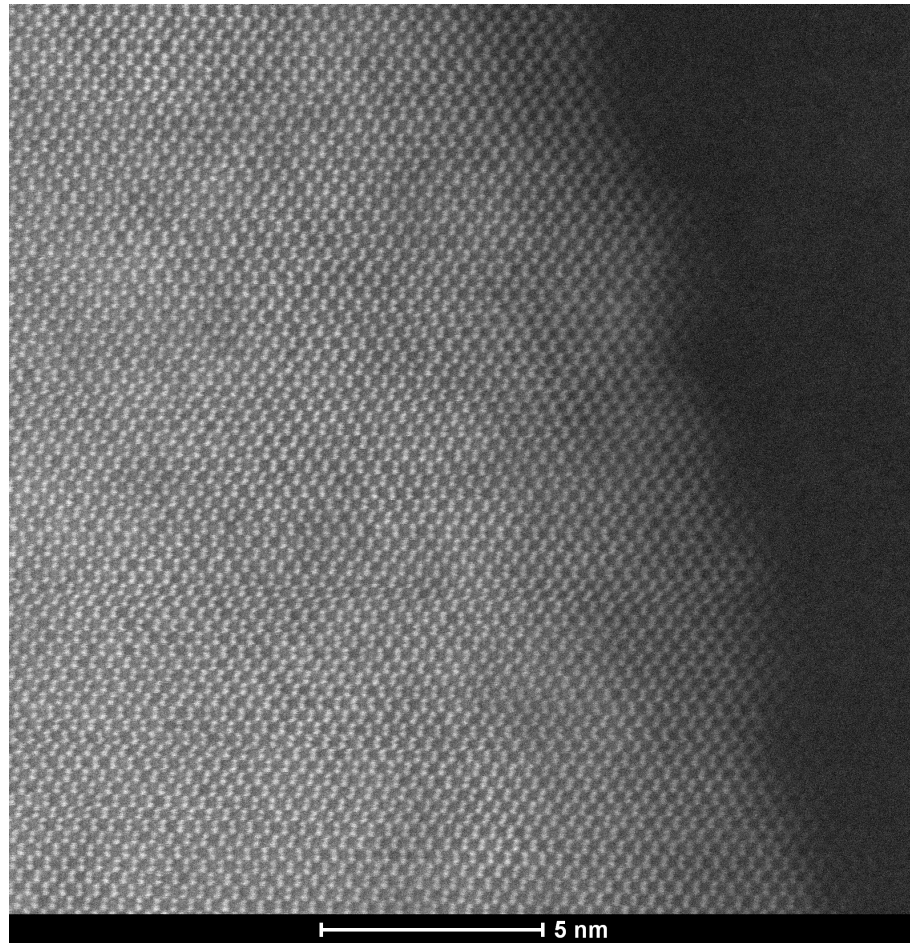
Figure 21: HR-STEM image of side of Ga$^+$ interaction

The sidewalls are particularly interesting as this is closer to the geometry that is used for thinning samples. Samples are not thinned by firing the beam directly at the sidewalls of the lamella; the beam is fired at a glancing angle to the sidewall. This is to reduce the amount of ions buried in the sample and help reduce lattice disruption and amorphisation.

It is clear why the Ga$^+$ FIB has become the standard for micro-nano machining and sample preparation. The Ga$^+$ LMIS is relatively stable and can produce high beam currents allowing for efficient neat cuts to be made in a range of materials. There are negatives though; a sample prepared completely from bulk to electron transparent using a high voltage 30kV Ga$^+$ ions will generally have defects introduced by the beam. There will be lattice disruption and the reactive Ga$^+$ ions implanted in the sample can cluster along grain boundaries, and even cause phase changes in the material [30]. Next, we will look at the interaction of He$^+$ ions with silicon.

6.4 Interaction of He⁺ ions in silicon

For the next study, our aim is to investigate the interaction of He^+ ions with a thick Si lamella. The bulk lamella is prepared using the procedure outlined the lamella preparation method section 6.2.1. The lamella was mounted into the Zeiss NanoFab in geometry so that the ion beam is incident on its top surface. A focused probe of He^+ ions, with a probe current of 33pA, is parked in several spots across the top of the lamella. The distance between the exposed regions was kept above 1 μm, to ensure that there is no crosstalk between exposed points. The probe dwelled for one second giving a total ion dose of 2.06×10^8 ions which works out to 6.57×10^{19} He^+ ions/cm² on points B and C while points A and D the probe dwelled for thirty seconds giving a total dose of 6.19×10^9 ions this works out to 1.97×10^{21} He^+ ions/cm². The ion doses are calculated from eq. 12.
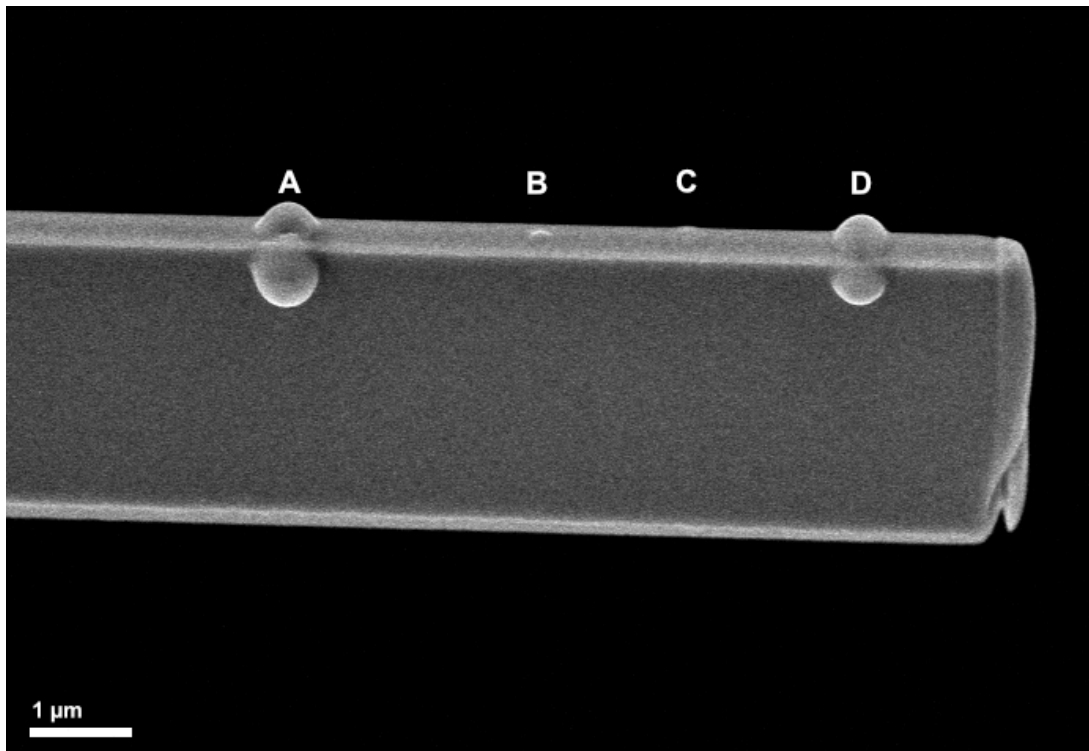
Figure 22: SEM image of the damage and swelling caused by the He^+ ion beam. Points A and D were exposed to a thirty second 1.97×10^{21} He^+ ions/cm² ion dose whereas points B and C received a one second 6.57×10^{19} He^+ ions/cm² ion dose.

When imaged in the SEM, the damage after ion irradiation is clearly visible as can be seen in figure 22. A striking characteristic observed after bombarding a spot on the silicon with the He^+

ion beam is a very noticeable swelling of the material. The blister-like structures protrude from both the surface and the sides of the lamella.

After the bulk sample was imaged in the SEM it was thinned using low voltage Ar^+ ions in a Fischione NanoMill. From the cross-section STEM image in figure 23, we can see that at a lower dosage of 6.57×10^{19} He^+ ions/cm^2 no material has been removed. In the impact zone the crystal structure has been disrupted and the material has become amorphous. Additionally, the structure is becoming partially porous at the bottom, suggesting that the damage penetrated hundreds of nanometres into the silicon.
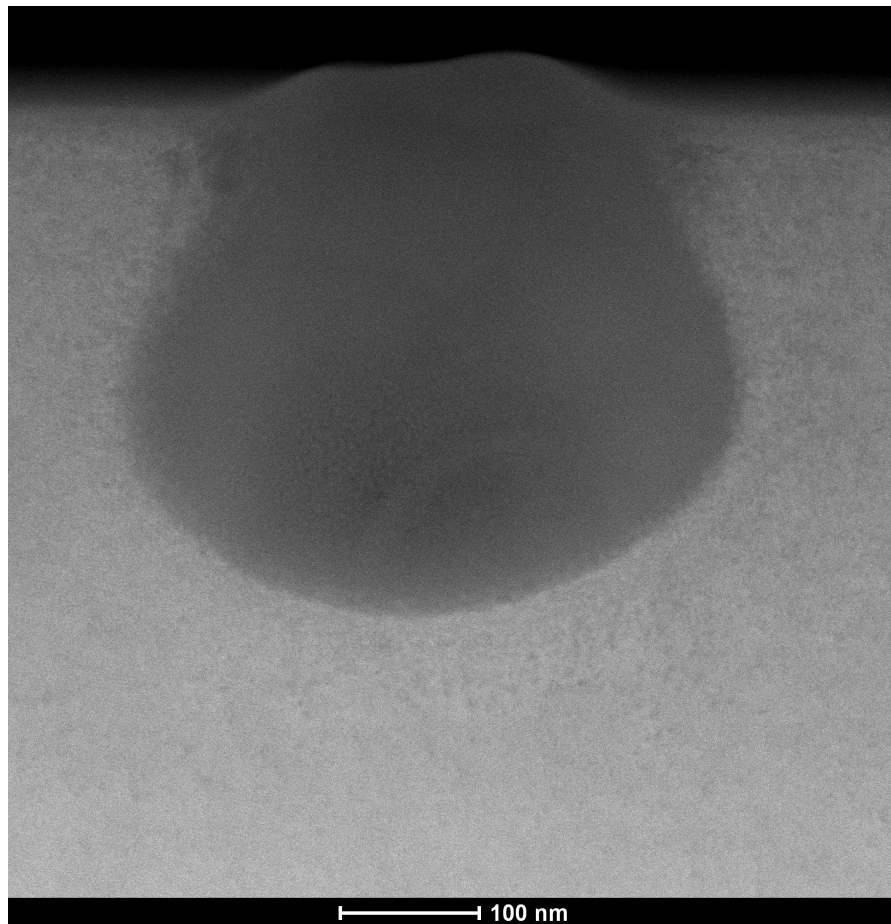
Figure 23: HAADF STEM overview image of the one second 6.57×10^{19} He^+ ions/cm^2 interaction.

At a depth of ~360nm, there are crystallites of the damaged silicon amongst the amorphous silicon before full crystallinity is restored. The same features are observed along the sides of the amorphous region as can be observed in figure 24.
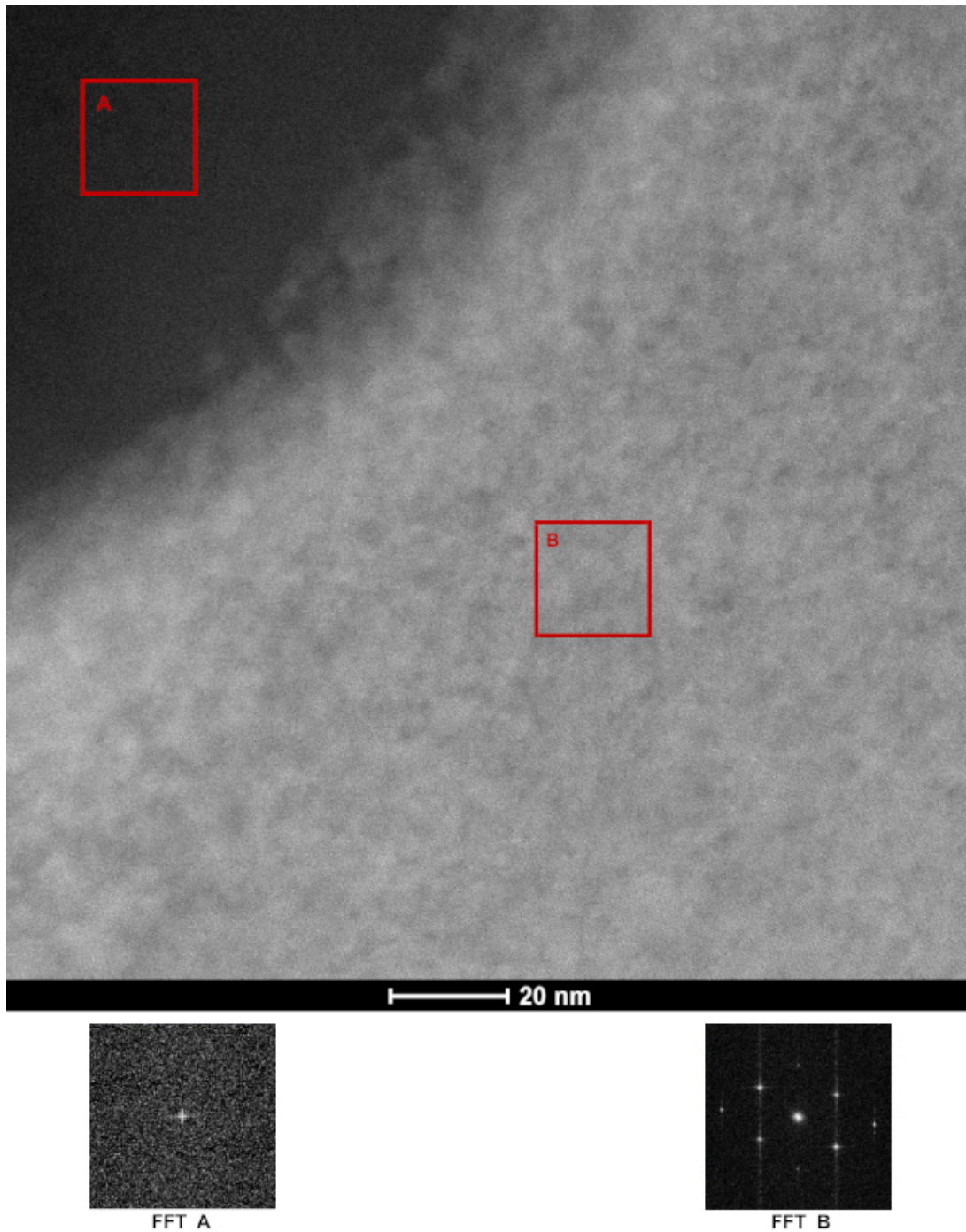
Figure 24: (a) STEM image at the sidewall of the one second 6.57 x 10^{19} He$^+$ ions/cm^2 interaction showing the interface transition from amorphous to fully crystalline, (b) FFT A shows the is no crystallinity in the amorphous region before the interface, and (c) FFT B shows the ordered single-crystal structure away from the interaction area bulk.

The HAADF STEM cross-section image of the 30 seconds 1.97 x 10^{21} He$^+$ ions/cm^2 interaction in figure 25, shows how the damage extends much further at ~1µm from the primary point of impact into the bulk of the Si, although no material has been removed. In the centre of the

impact, a large egg-shaped porous structure is formed. The largest voids are in the centre of the structure at ~80nm in diameter, the void size consistently reduces until turning into a solid amorphous silicon layer. The porous structure has caused serious surface swelling and the centre of the interaction area protrudes ~200nm above the top surface of the sample.
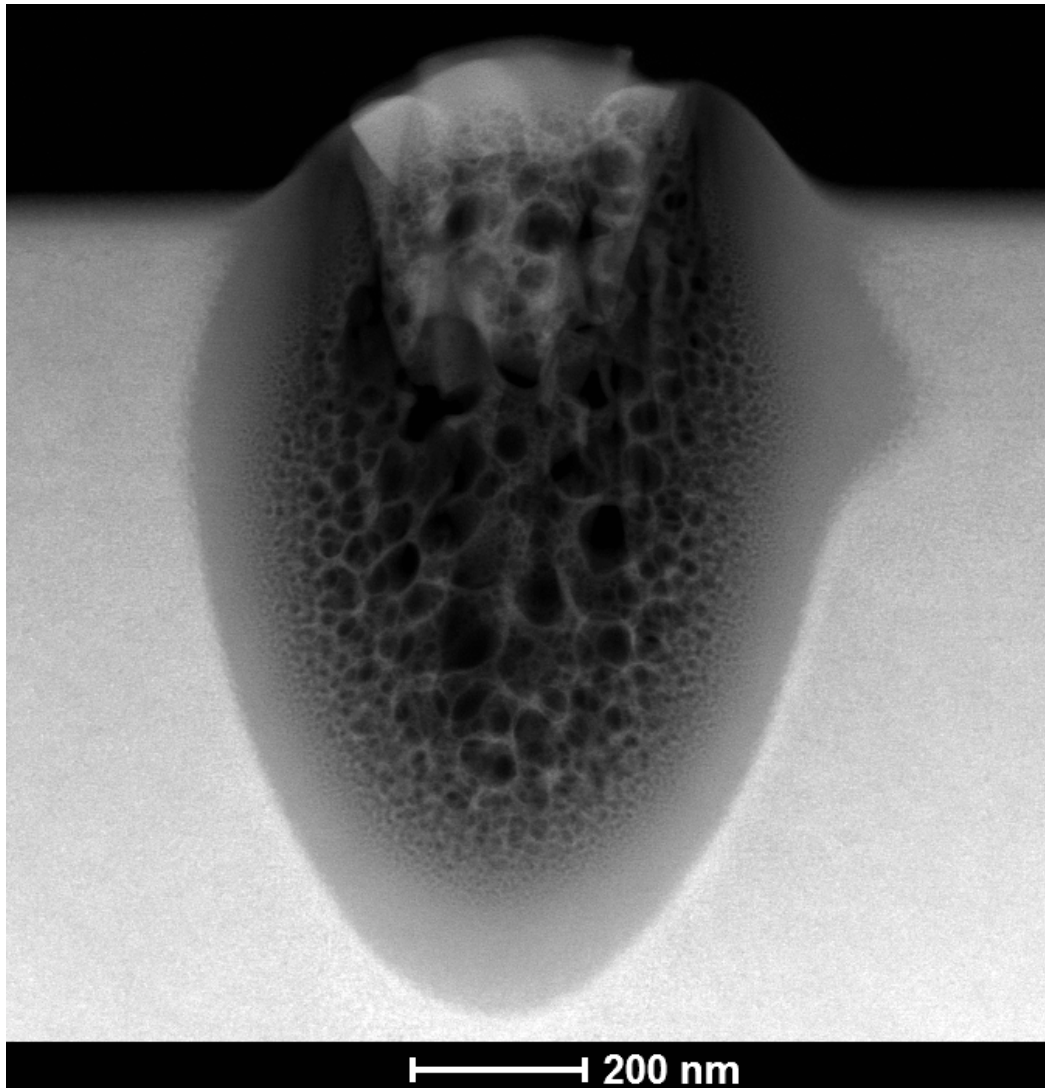
Figure 25: Cross-section HAADF STEM image of point A, the thirty second 6.57 x 10^{19} He$^+$ ions/cm^2 interaction

The porous structure is surrounded by ~50nm of amorphous silicon. The interface of amorphous silicon and crystalline silicon is similar to the lower dose 6.57 x 10^{19} He$^+$ ions/cm^2 impact where there are small crystallites ~5nm amongst the amorphous silicon before full crystallinity is restored. This can be clearly observed in figure 26.

FFT A   FFT B
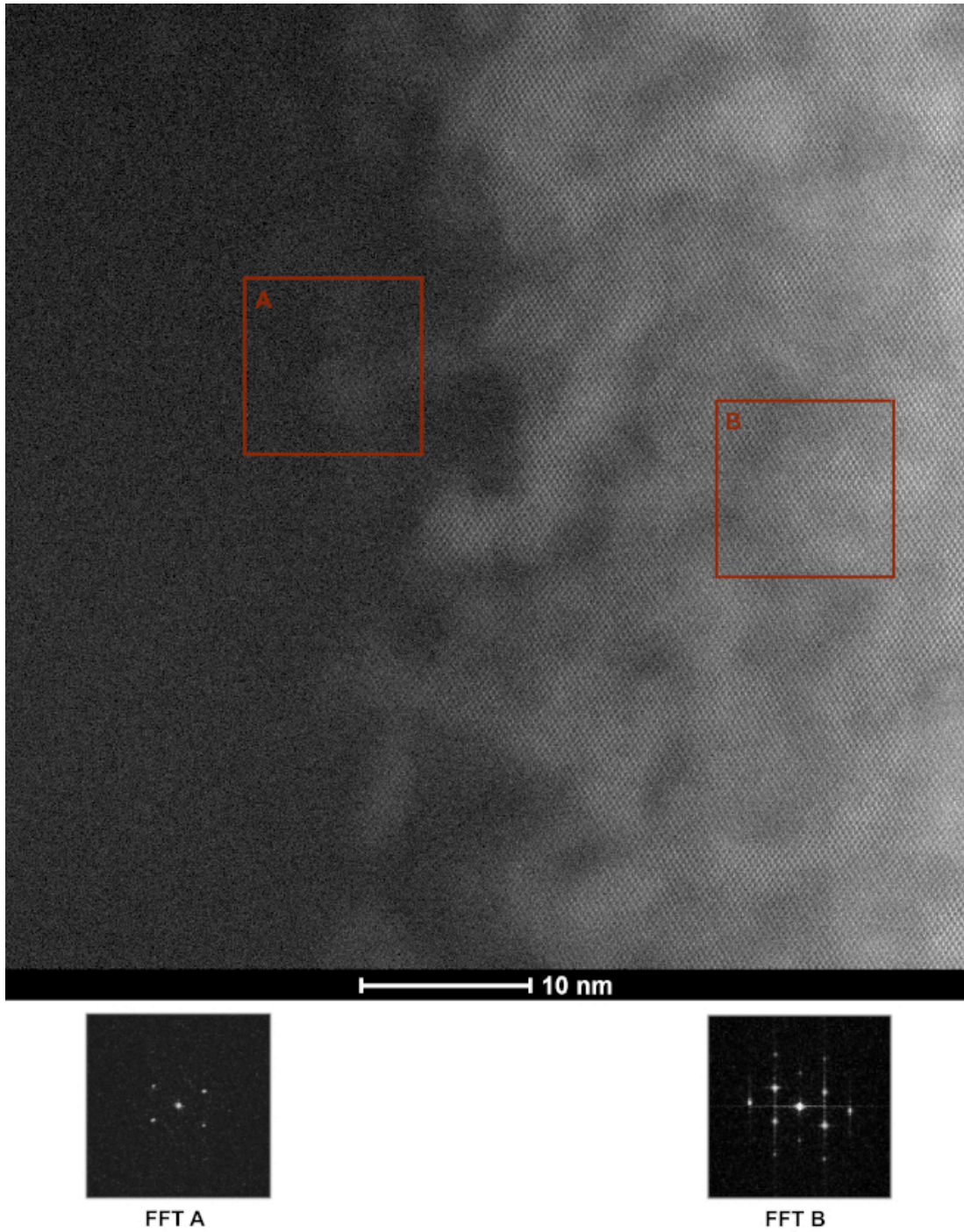
Figure 26: HAADF HR-STEM image of the side of the amorphous region returning back to crystalline silicon. FFT A shows structure to the crystallites at the interface from amorphous to crystalline, FFT B shows the ordered single-crystal structure returning

Electron Energy-Loss Spectroscopy (EELS) was performed at the edge of the ion interaction area at the transition of the porous to the amorphous region on the 1.97×10^{21} He$^+$ ions/cm^2 interaction. As can be seen in the EELS map, figure 27 (b), Si is detected in both the solid amorphous region and in the porous structure, SiO$_x$ is detected in the porous structure only,

this is due to the large surface area created by the porous structure and a thin native oxide forming.
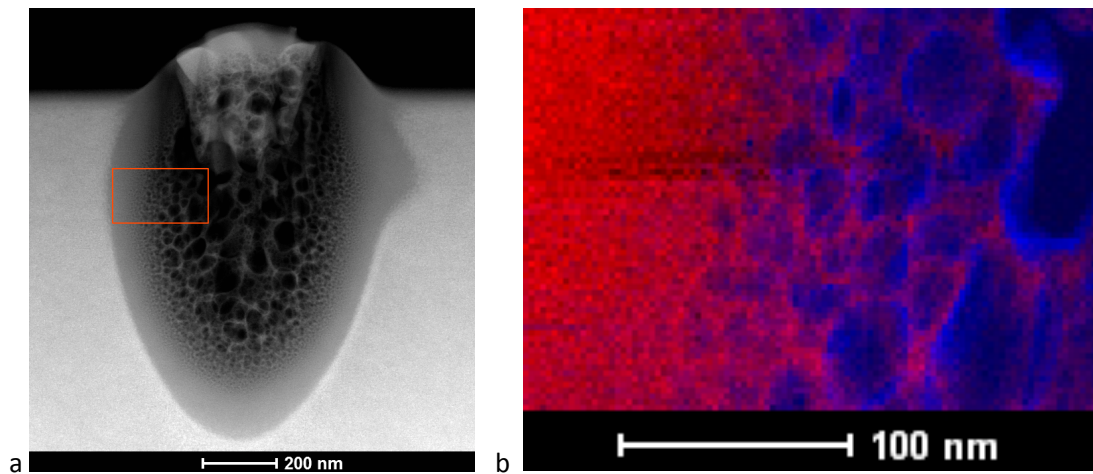
Figure 27: (a) The side of the amorphous region HAADF STEM image of cross-sectioned and 1.97 x 10^{21} He$^+$ ions/cm^2 interaction and (b) EELS map showing Si edge in red and SiO$_x$ edge in blue

The damage observed from the He$^+$ ion interaction is not the kind of damage we expect from an ion beam [15] (p55). Generally when an ion beam is accelerated at a surface material is removed, but the light He$^+$ ion beam does not remove material at the surface of the silicon. As previously calculated from eq. 5, a 30kV He$^+$ ion's velocity is more than four times that of a Ga$^+$ ion. Travelling at a greater velocity, the ion penetration depth increases, causing the ion to travel further into the bulk and experience many electronic interactions before eventually having a nuclear interaction and causing damage beneath the surface. The issue is when the light ion is displacing an atom it is far away from the surface so instead of removing material, the ion disrupts the structure of the sample. Another effect of the large number of electronic interactions is localised heating. With the light ions heating up the area and atoms being displaced beneath the surface, the He$^+$ ions can cluster to form small bubbles of gas. This could be the reason a porous structure is produced and the sample starts to swell. The sputter yield for He$^+$ ions is so low by the time some material is removed, many of ions are implanted into the bulk, causing swelling and damage. This effect is also observed for heavier elements [31]

We have looked at He$^+$ ion interaction, we will now investigate another ion species to look at its viability for sample preparation. In the following section, we will look at the interaction of Ne$^+$ ions with silicon.

6.5 Interaction of Ne$^+$ ions in silicon

The next ion species investigated was Ne$^+$. The lamella was fabricated using the technique outlined in the lamella preparation method section 6.2.1. The lamella is mounted into the Zeiss NanoFab with a beam geometry incident to its top surface. A focused probe of Ne$^+$ ions, with a probe current of 31pA, is parked in several spots across the top of the lamella. With a dwell time of 1 second, points A and B were exposed to an ion dose of 4.28×10^{17} Ne$^+$ ions/cm^2. Point C had a dwell time of 30 seconds giving a dose of 1.29×10^{19} Ne$^+$ ions/cm^2. The ion doses are calculated from eq. 12.
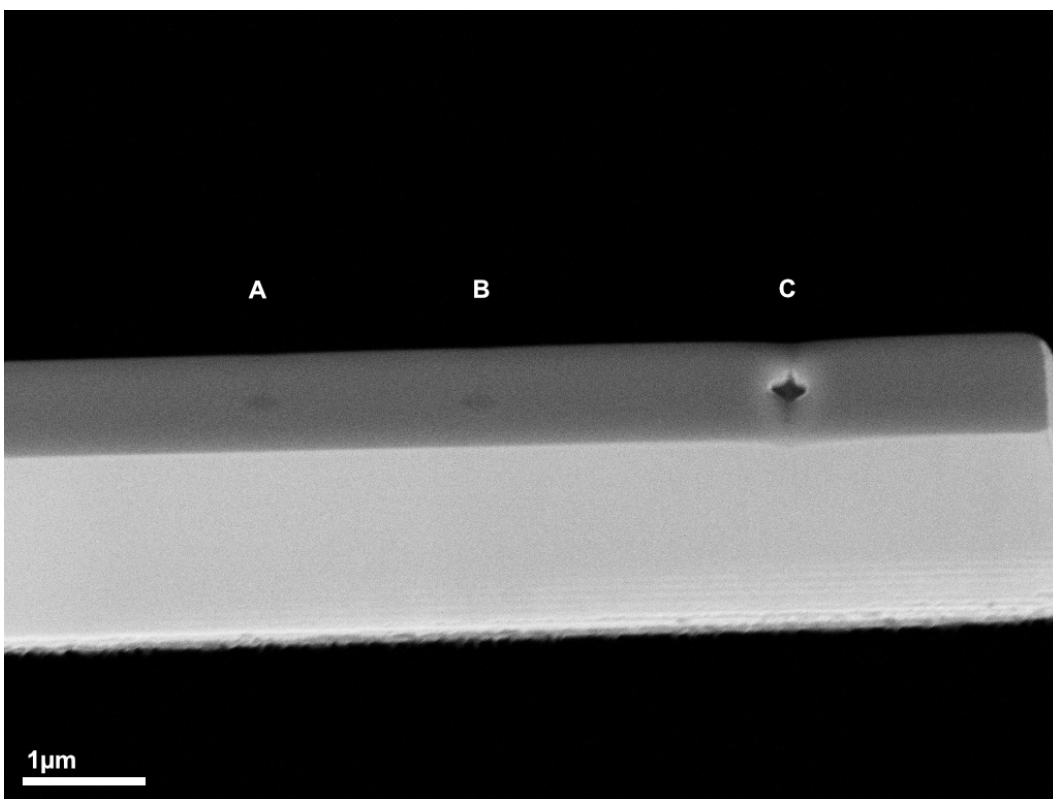
Figure 28: SEM image, displaying the Ne$^+$ ion interactions on the lamella. Spots A and B the lower dosage 4.28×10^{17} Ne$^+$ ions/cm^2 are barely visible, while Spot C the higher ion dose of 1.29×10^{19} Ne$^+$ ions/cm^2 is clearly visible and some material has been removed.

As mentioned in the materials and methods section 6.2, the bulk lamella was thinned using low voltage Ar$^+$. Both sides were thinned with identical parameters to reveal the centre of the ion impact. The sample is then imaged in HAADF STEM.

From the cross-section STEM image in figure 29, we see no material has been removed at the lower dosage spot A 4.28×10^{17} Ne$^+$ ions/cm^2. However, the crystal structure has been

disrupted and turned the crystalline Si amorphous. Near the surface, the porous structure is just beginning to form.
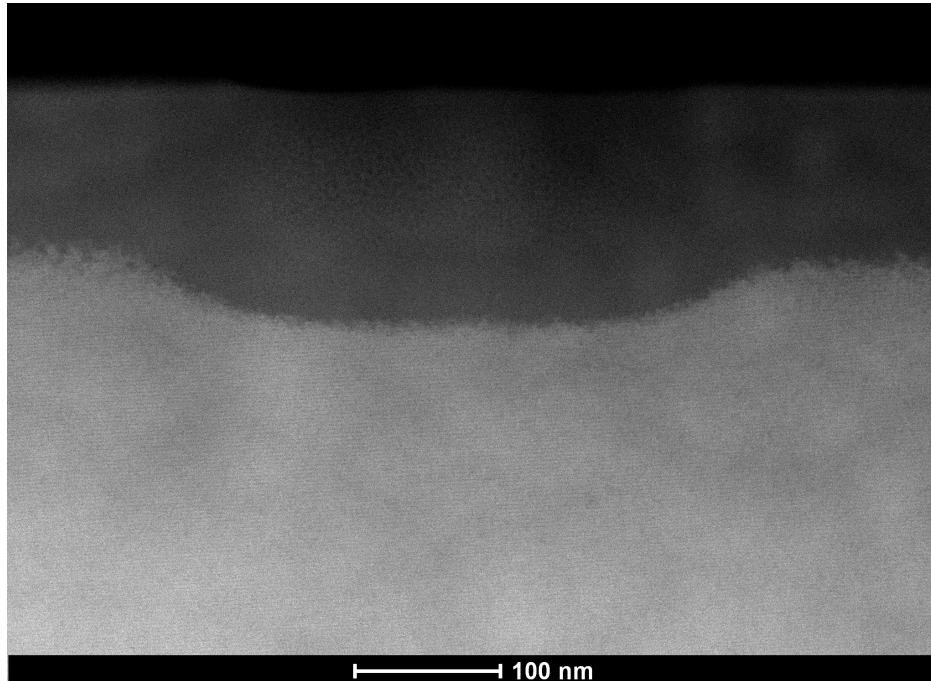

Figure 29: A HAADF STEM image of the lower dose 4.28×10^{17} Ne$^+$ ions/cm^2 interaction in Si at spot A

In figure 30 the HAADF STEM image shows the larger 1.29×10^{19} Ne$^+$ ions/cm^2 ion dose spot C. The Ne$^+$ ions are significantly more successful at removing material than the He$^+$ ions, as can be seen from the pit formed at the surface in figure 30. Although the Ne$^+$ removes material better than He$^+$ milling, the silicon experiences similar sub-surface damage. The damage extends hundreds of nanometres into the bulk creating porosity in the silicon. At the surface, there are large voids ~100nm. It appears these voids eventually get eroded away, creating a small pit in the surface of the silicon. At the center of the impact zone, large voids are created, over a short distance ~10nm, the pore size reduces dramatically. These voids consistently reduce in size until the porous material becomes a solid layer of ~50nm amorphous silicon before full crystallinity is restored.
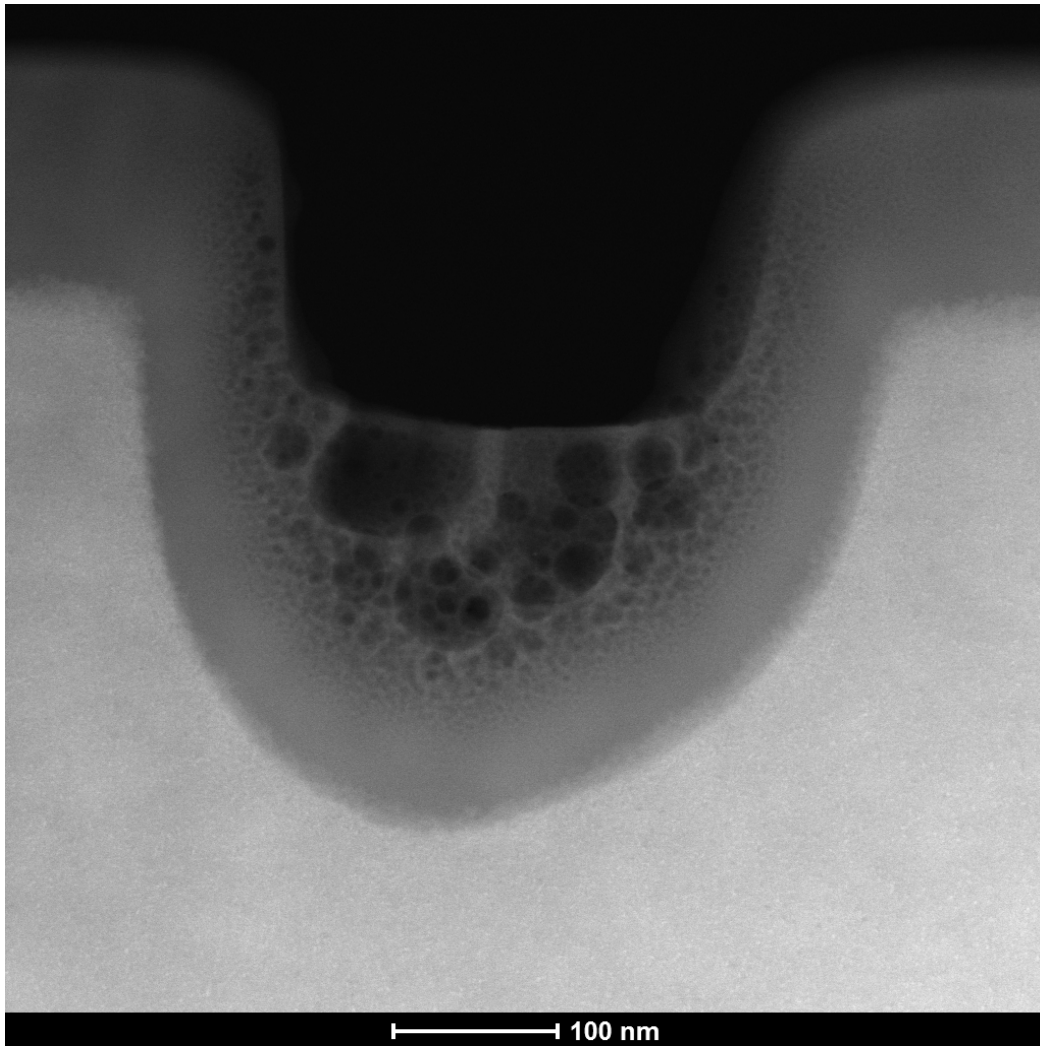
Figure 30: A HAADF STEM image of the 30 second 1.29 x 10^{19} Ne$^+$ ions/cm^2 dose at spot C

Figures 31 and 32 show that the interface from amorphous to crystalline is similar to the He$^+$ ion interaction. Small crystallites 2-5nm and sporadic crystallinity decorate the interface from amorphous to fully crystalline silicon.
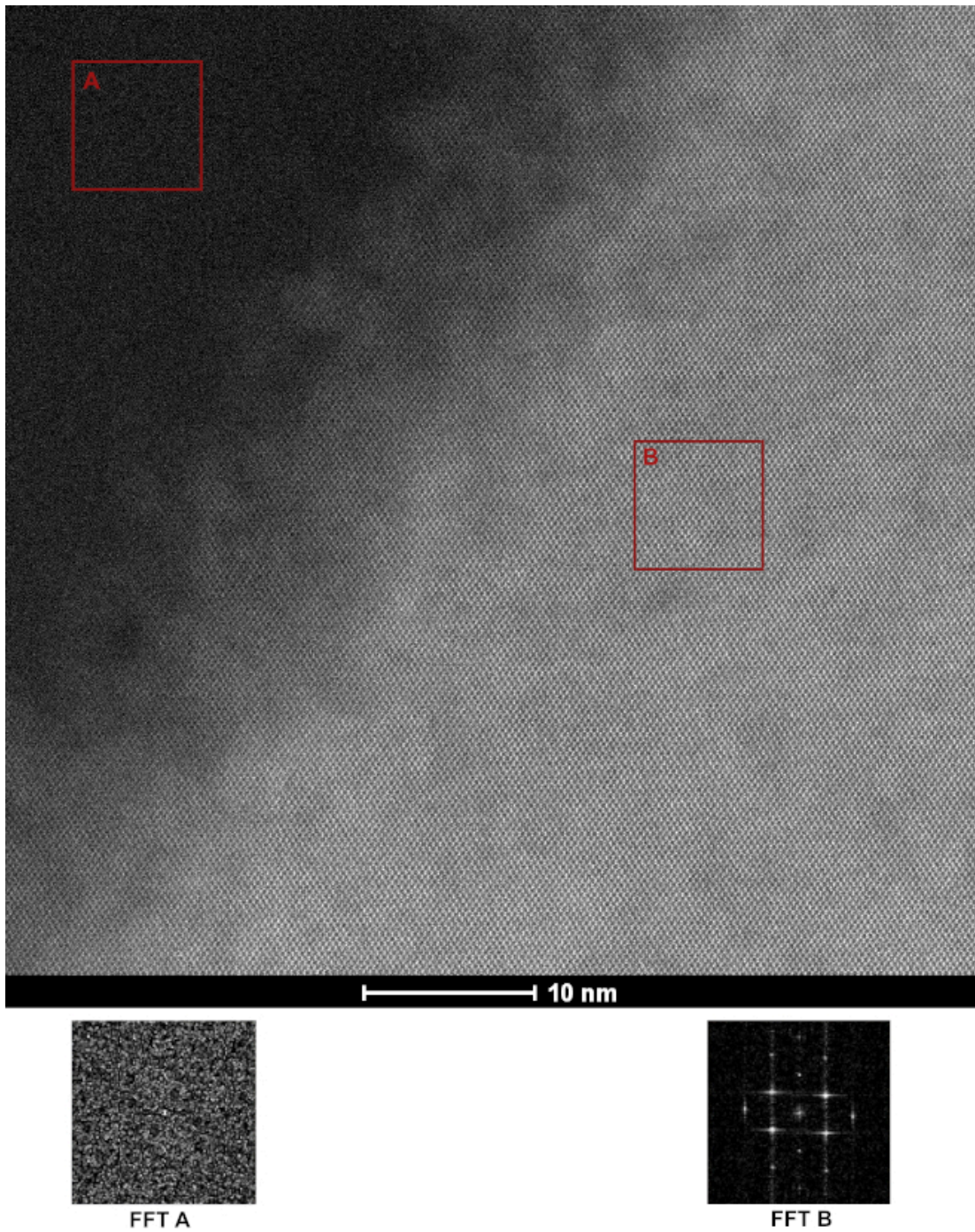
Figure 31: HR-STEM image of the side of the amorphous region (spot C) returning back to crystalline silicon. FFT A shows the is no crystalline structure in the amorphous region before the interface, FFT B shows the ordered single-crystal structure in the bulk
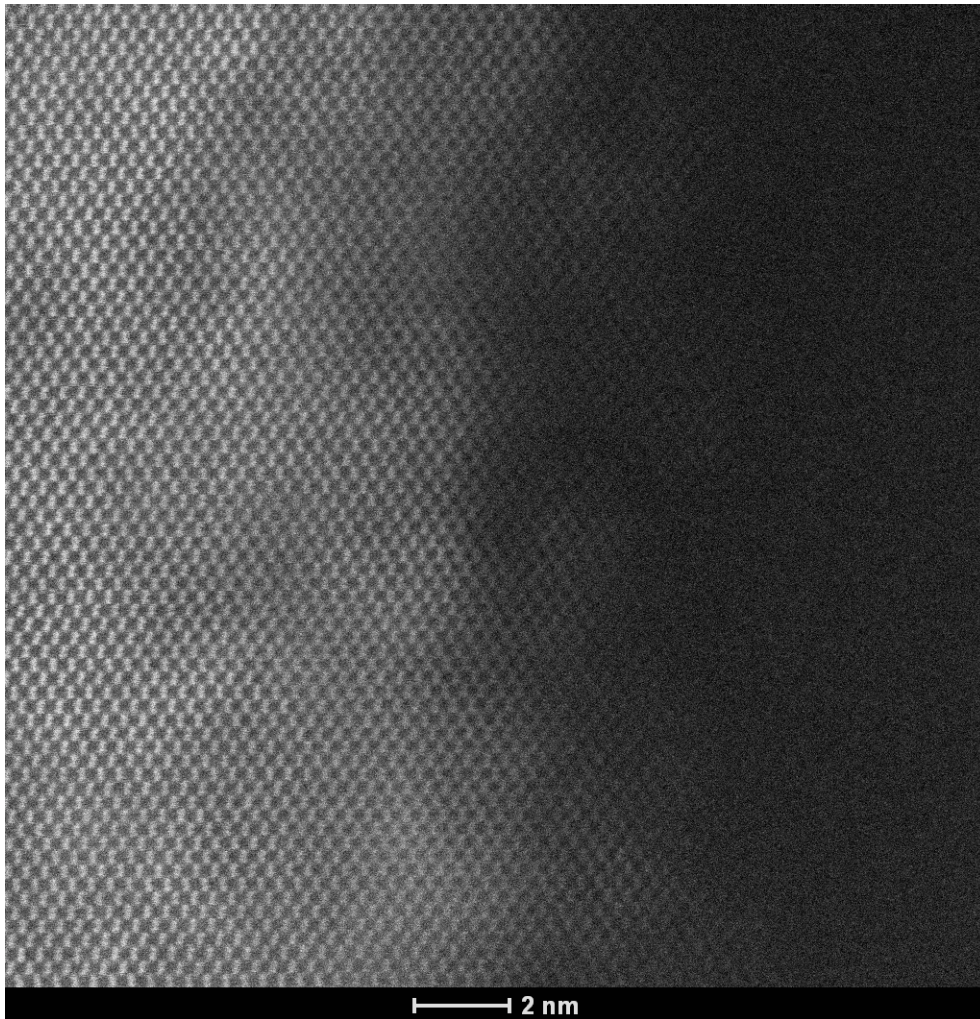
Figure 32: HR-STEM image of the interface between amorphous and crystalline silicon (spot C), crystallites and sporadic crystallinity can be observed at the interface.

Although the Ne$^+$ ions are heavier than the He$^+$ they are still travelling at a significantly higher velocity than Ga$^+$; this creates a hybrid of the two interactions we have observed so far where the Ne$^+$ ions travel into the silicon and create damage beneath the surface but unlike the He$^+$ ions manage to remove some material.

Next, we will investigate the interaction of Ne$^+$ ions in silicon at a lower accelerating voltage. The theory of which was discussed in the ion theory section 3.

6.6 Low Voltage Ne$^+$ ion interaction

In this section we investigate the interaction of low voltage Ne$^+$ ions accelerated at 8.6kV with silicon. As discussed in the theory section, an 8.6kV Ne$^+$ ion will have the same velocity as a 30kV Ga$^+$ ion. The lamella is fabricated using the technique outlined in the lamella preparation method section 6.2.1, it was then mounted into the Zeiss NanoFab with a beam geometry incident to its top surface. The top surface of the lamella, was exposed to a focused probe of Ne$^+$ ions, accelerated at 8.6kV with a probe current of 11pA. A dwell time of 90 seconds was used to give a dose of 4.66 x 10^{19} Ne$^+$ions/cm^2. The ion dose is calculated from eq. 12.
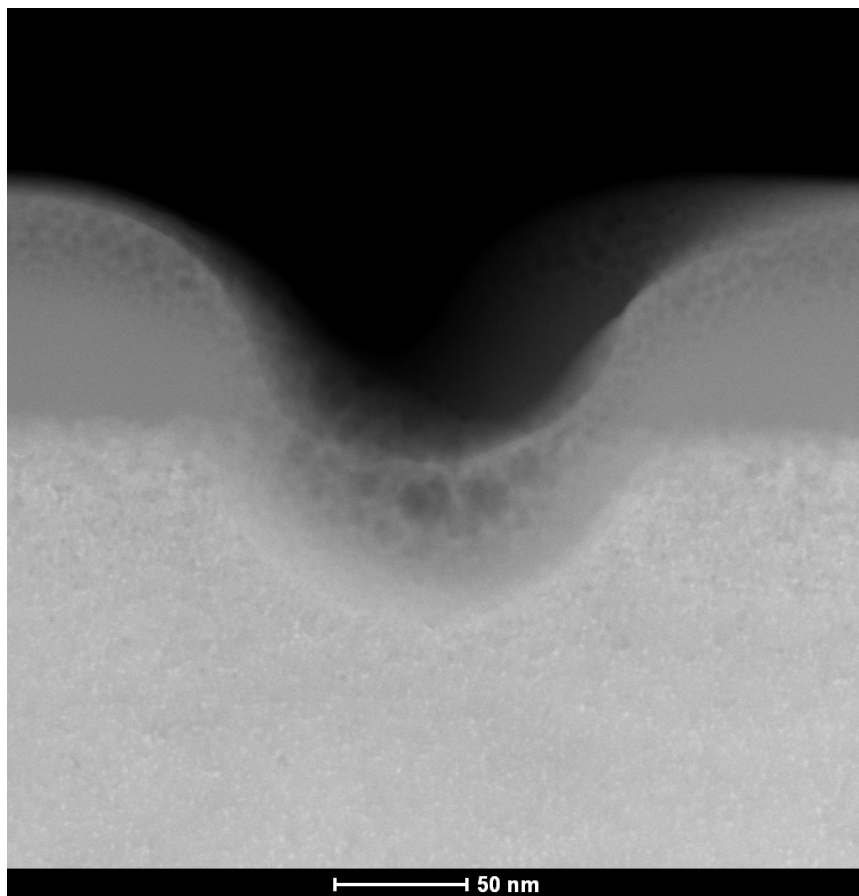
Figure 33: A HAADF STEM image of the 4.66 x 10^{19} Ne$^+$ions/cm^2 interaction

In figure 33 we can see the interaction of the lower voltage Ne$^+$ looks similar to the 30kV Ne$^+$ figure 30. A small amount of material has been removed; however there is still bubbling, void formation and an amorphous layer. Compared to the 30kV Ne$^+$ interaction the damage layer from the 8.6kV Ne$^+$ has been reduced from ~200nm to ~50nm. There is a much cleaner interface between the amorphous and crystalline silicon. This can be seen in figures 34 and 35.

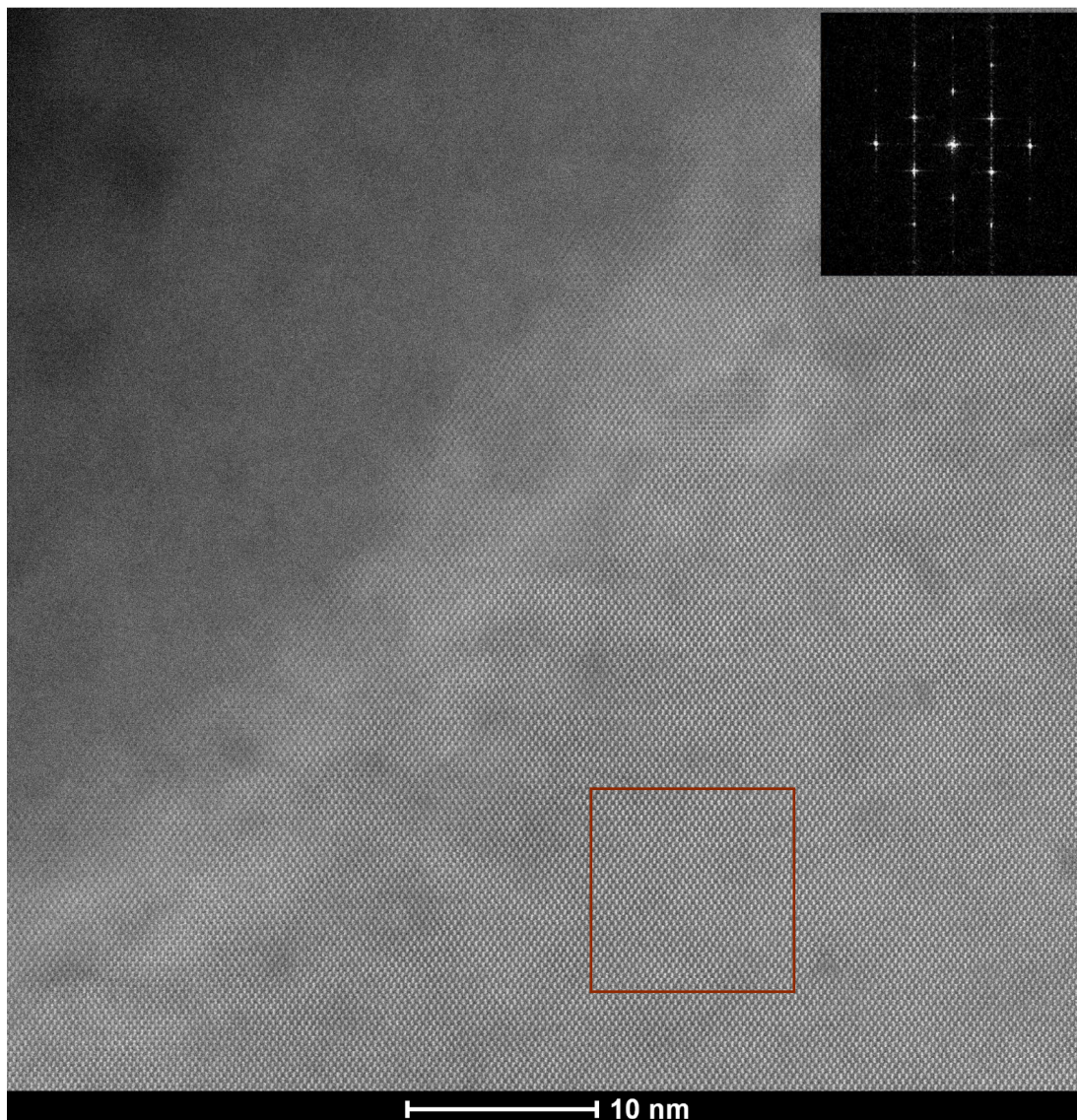**Figure 34:** HR-STEM image of amorphous silicon interface to crystalline silicon. FFT inset from area highlighted in red shows good crystallinity
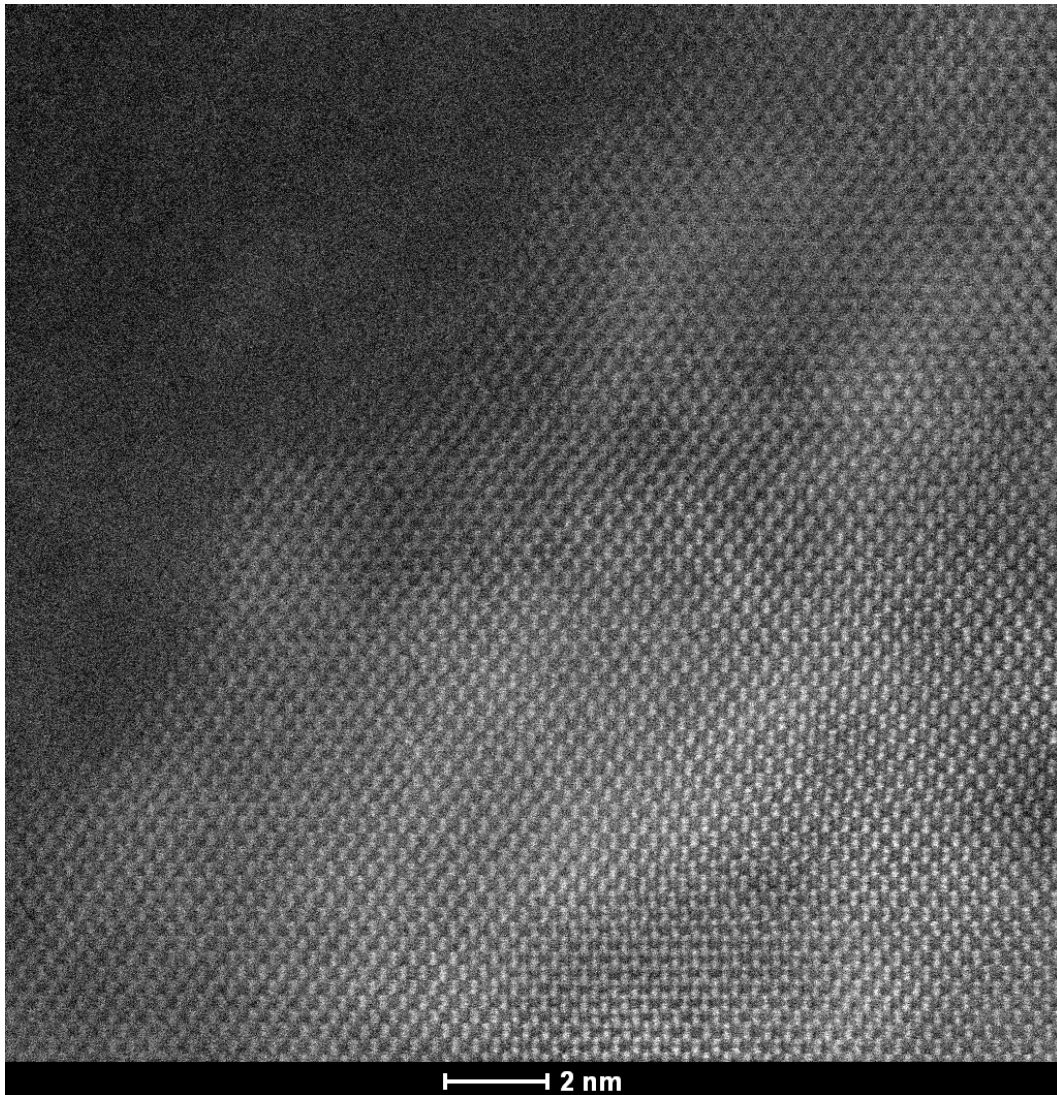
Figure 35: HR-STEM image of amorphous to crystalline silicon interface

Although the Ne$^+$ ions are interacting with a reduced velocity there is still significant surface damage and disruption to the crystalline structure. A downside to lowering the voltage is the beam current is also reduced this would make it very time consuming to thin samples.

6.7   Ion polisher low voltage Ar$^+$ ion interaction

The Nanomill has been used for all the final thinning and polishing of the samples analysed thus far. Therefore for completeness, in this section of experiments, cross-section images of the low voltage Ar$^+$ ion interaction from the Fischione NanoMill were acquired. The bulk lamella is fabricated using the technique outlined in the materials and methods section 6.2. The lamella is mounted into the Fischione NanoMill with a beam geometry incident to its top surface. For a dwell time of 10 minutes, a focused beam of Ar$^+$ ions accelerated at 900V with a probe current of 92pA is exposed to the top surface giving a dosage of 1.1 x 10^{19} ions/cm^2. The probe produced by the NanoMill is much larger than the other instruments, measuring at ~2μm. Therefore, the current density per unit area is lower than that of the other instruments and will require a longer time to mill a spot.
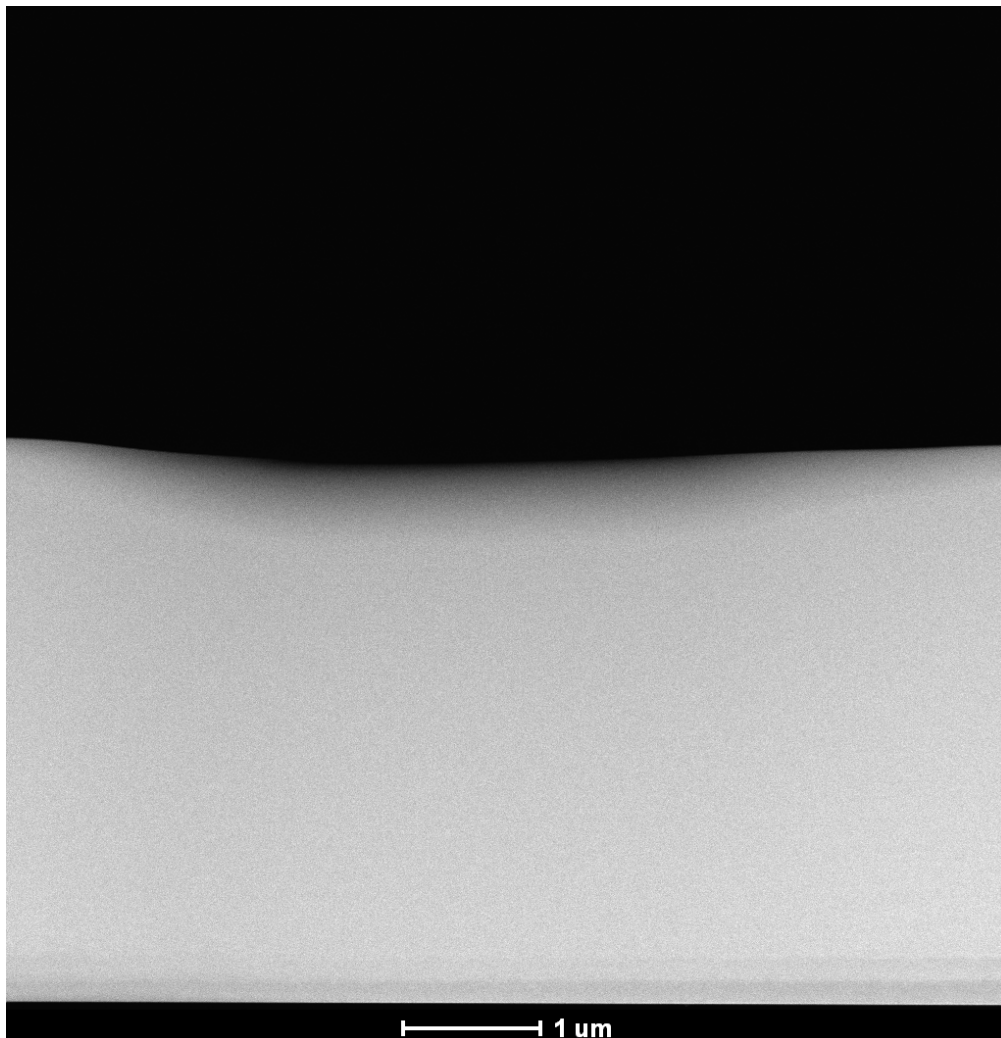

Figure 36: HAADF STEM of a shallow pit formed from the Ar$^+$ ion interaction

Figure 36 shows a shallow pit formed by the Ar$^+$ ion interaction milling into the top surface of the Si lamella. Figure 37 is a high-resolution STEM image from the base of the pit. There is ~5nm of amorphous silicon leading into a pristine crystalline Silicon interface containing no crystallites. considering that this the result of the incident beam interacting normal to the sample surface at zero degrees tilt it still gives a good finish with a clean interface.
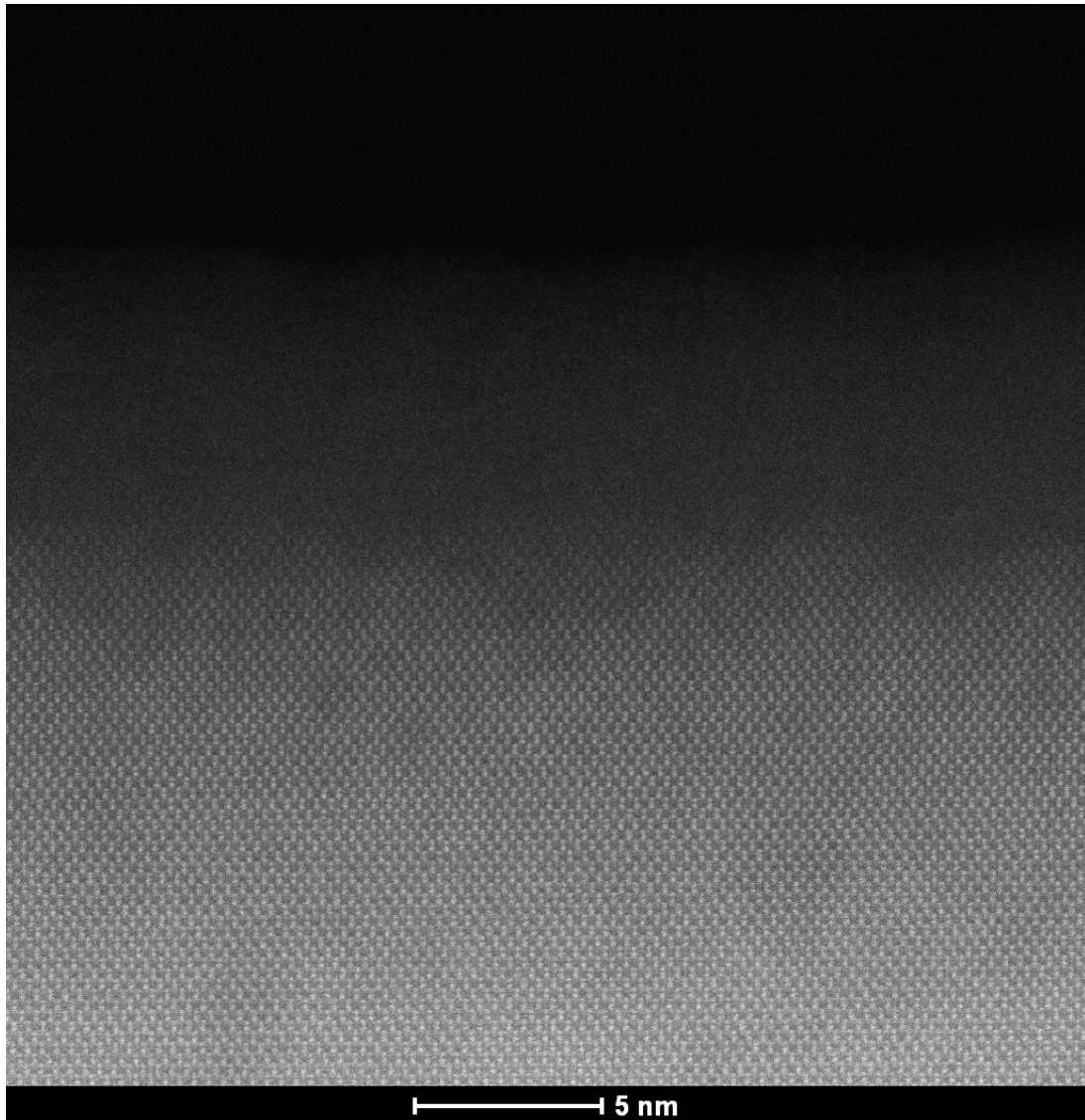

Figure 37: HAADF STEM of the bottom of the pit formed by the low voltage Ar$^+$ interaction

As we can see in the images above the NanoMill working at very low accelerating voltages with a slightly heavier inert gas ion, gives a very good finish with very little surface damage. This makes it a useful instrument for the final thinning and polishing of lamellae for high-resolution electron microscopy.

6.8   SRIM Simulation

To help understand the experimental results of the light ion interaction we have seen so far simulations were performed using SRIM. As described in the theory section 3 the interactions between ions and bulk material can be modelled using software. The software used here is SRIM (stopping range of ions in matter). SRIM is a Monte Carlo simulation using BCA (binary collision approximation) which maps each ion's stopping distance and trajectory as it travels into the sample. The path of each ion can be displayed in an image, and when enough ions have been simulated, the image provides an approximation of the interaction depth and volume for the selected ion species.

The simulations were performed using the relevant ion species and accelerating voltage for 1500 ions fired at 0° tilt into the surface of silicon. The models produced were then scaled correctly and overlaid on the experimental data as a visual comparison between simulation and experimental results. Exceeding 1500 ions in the simulation not generate any more information for the purpose of the qualitative analysis data displayed in this section. As can be seen in figure 38, the bulk interaction pattern (highlighted in red) is saturated.

As can be seen in figure 38 the He$^+$ ion simulation fits quite well over 6.57 x 10^{19} He$^+$ ions/cm^2 interaction experimental data. The simulation was performed using identical parameters detailed in the He$^+$ ion section of the experimental chapter.
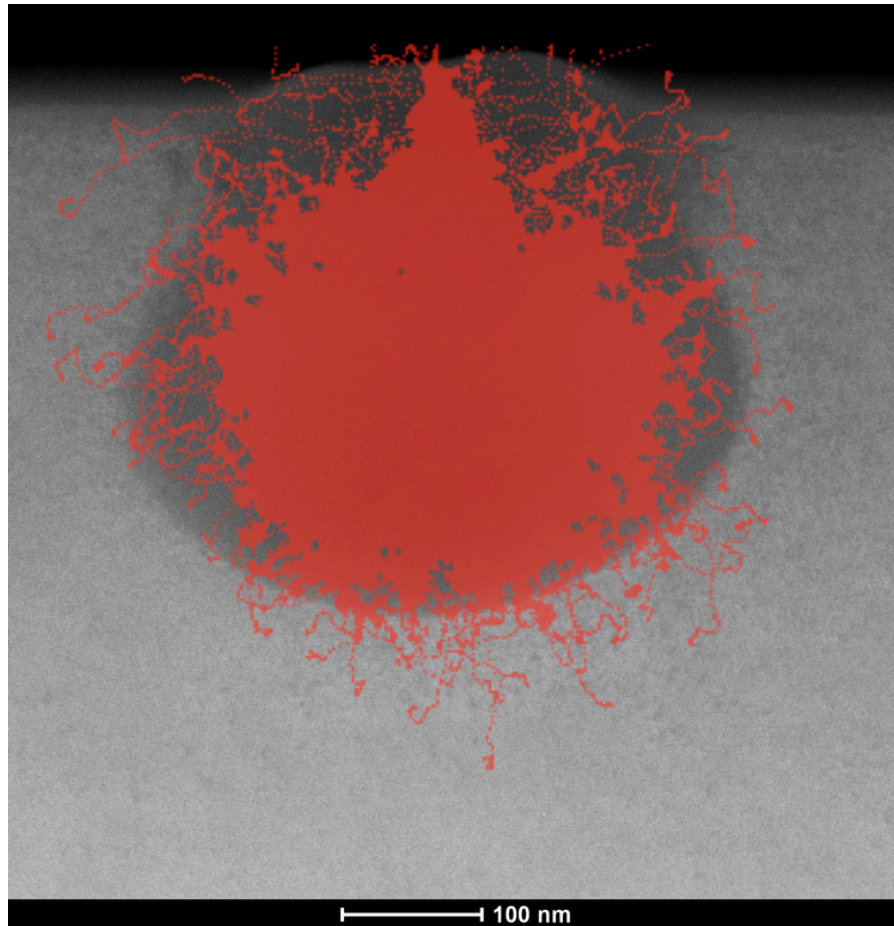
Figure 38: Low dose 6.57 x 10^{19} He$^+$ ions/cm^2 interaction with SRIM simulation data overlaid

For lower doses, the SRIM simulations mirror the experimental results quite well. As a result, this is a useful tool to understand where and how much damage will occur with the different ion species at different voltages. One area where the software fails in matching simulations with experimental data is the evolution of the sample as damage occurs. As the lighter ions cause significant sub-surface damage, generating porosity, they scatter out further into the sample causing even more damage even deeper into the material. Figure 39 (a), shows the same simulation as figure 38 but is overlaid onto the higher dosage He$^+$ ion interaction, as can be seen the damage is about twice the distance of the simulation. To see if a better fit from the simulation could be produced voids were manually added to Si target material in SRIM, this was done in a rudimentary way by adding thin layers of gas and silicon to simulate voids. As can be observed in figure 39 (b), the modified material gives a closer representation of the experimental result. To simulate larger ion interactions for light ions would require the software to constantly modify the material with increasing ion dose thereby creating lower

53

density regions and voids in the material. This would become very complex, particularly when modelling the bubble and void formation.
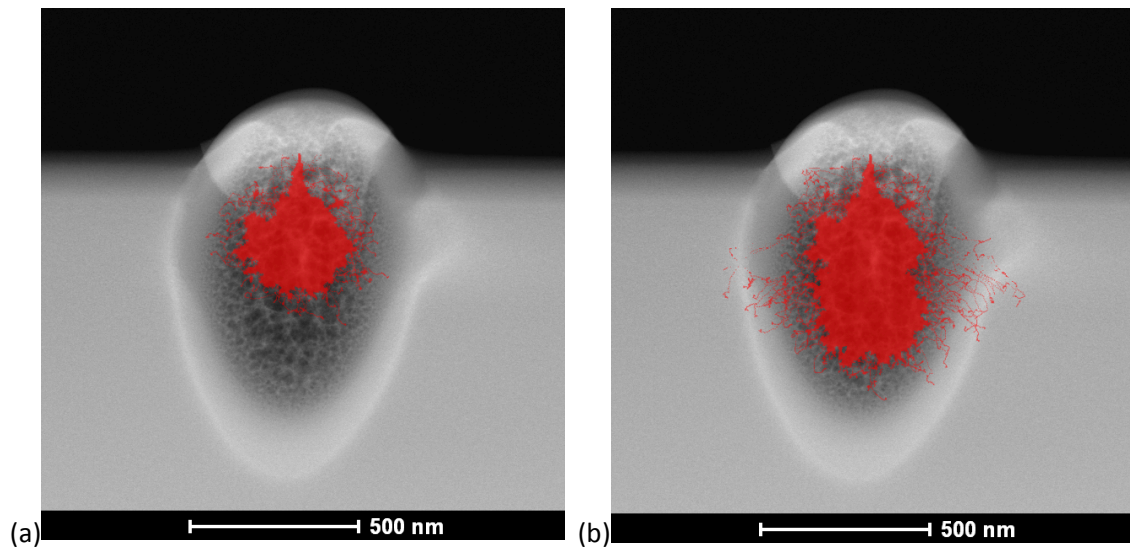

Figure 39: (a) Standard SRIM simulation overlaid on 30 second 1.97 x 10^{21} He$^+$ ions/cm^2 dose (b) SRIM simulation with voids added to material overlaid on 30 second 1.97 x 10^{21} He$^+$ ions/cm^2 dose

The Ne$^+$ ion beam is approximately 4 times larger than the He$^+$ ion beam, according to instrumentation specifications, although experimentally, this can vary. Also, due to the fact the Zeiss Nanofab was aligned for high beam current rather than resolution, using the largest aperture and adjusting the condenser lens the beam was around ten times bigger than the He$^+$ ion beam. SRIM performs simulations based upon a 1-dimensional probe entering into the sample surface [32]. For the Ne ion SRIM simulations, multiple simulations were placed overlapping next to each other to represent the larger probe interacting with the silicon. This was overlaid on the low dose of 4.28 x 10^{17} Ne$^+$ ions/cm^2 interaction image, as can be seen in Figure 40.
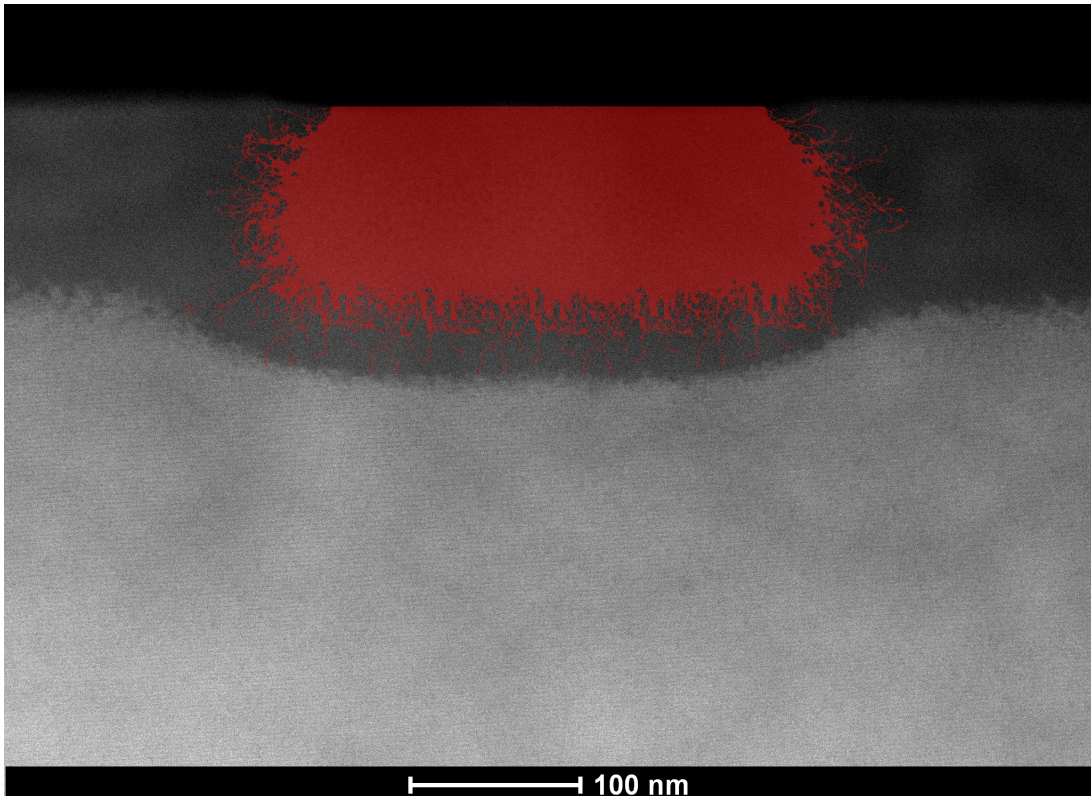
Figure 40: low dose 4.28 x 10^{17} Ne$^+$ ions/cm^2 interaction in silicon with SRIM overlay

Using the same technique as used for He ion simulation to add voids to the material, layers were introduced into the Si target material for the Ne ion simulation. Figure 41(a), shows a standard SRIM simulation overlaid on the 30 second 1.29 x 10^{19} Ne$^+$ ions/cm^2 interaction. Figure 41(b), shows a SRIM simulation with voids added to the Si target material. Displaying a similar result to the He ion modified simulation, the addition of voids to the target material simulation produces a closer match to experimental data. As can be seen in both Figure 41 (a) and (b), at the bottom left of the experimental interaction, it appears as though the beam penetrates approximately 20nm further into the bulk material. This effect might be caused by experimental issues, such as possible asymmetry in the probe (residual astigmatism and low order aberrations).
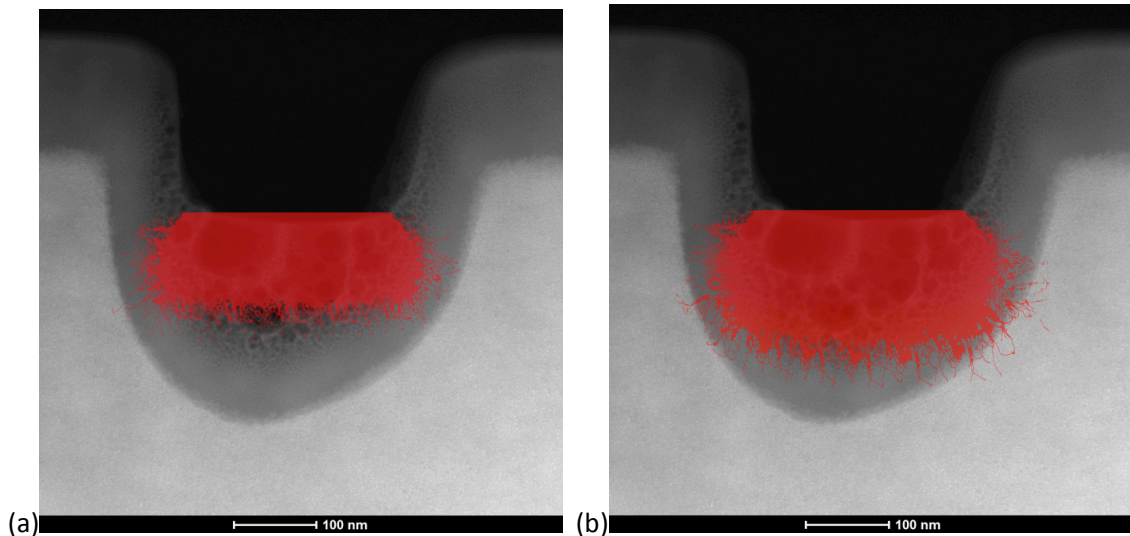
(a)   100 nm   (b)   100 nm

Figure 41: (a) Standard SRIM simulation overlaid on 30 second 1.29 x 10^{19} Ne$^+$ ions/cm^2 interaction (b) SRIM simulation with modified material overlaid on 30 second 1.29 x 10^{19} Ne$^+$ ions/cm^2 interaction

The SRIM simulation also allows us to plot the atomic displacement over depth for the different ion species. The graph in figure 42 shows the atomic displacement of silicon against depth for different ions He$^+$ Ne$^+$ and Ga$^+$ all accelerated at 30kV. The displacement ratios were normalised, as they were different for each ion species.
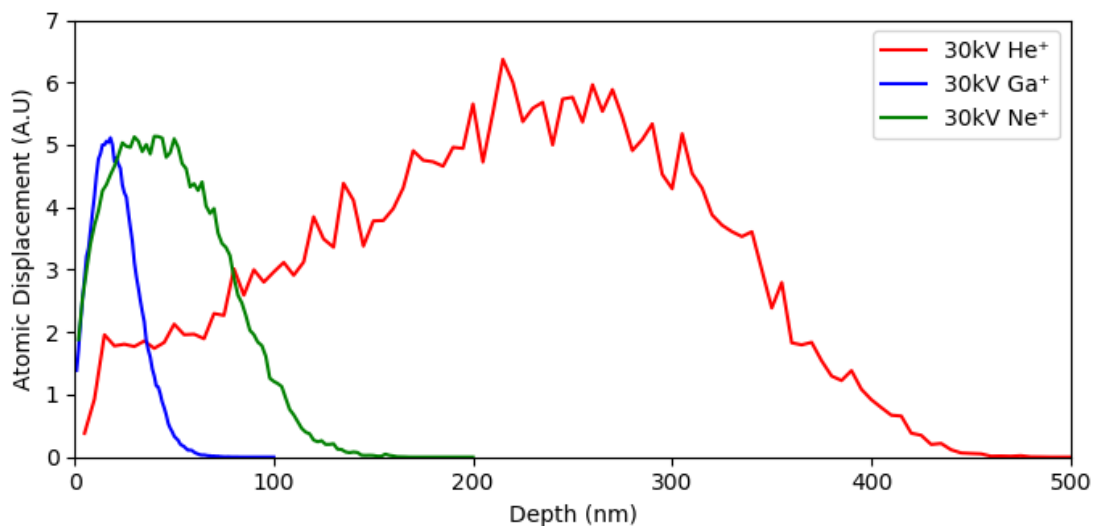

Figure 42: SRIM data showing atomic displacement of silicon over depth

The graph below in Figure 43 shows the atomic displacement against depth for Ga$^+$ and Ne$^+$ at 30kV, Ne$^+$ at 8.6kV and Ar$^+$ at 0.9kV
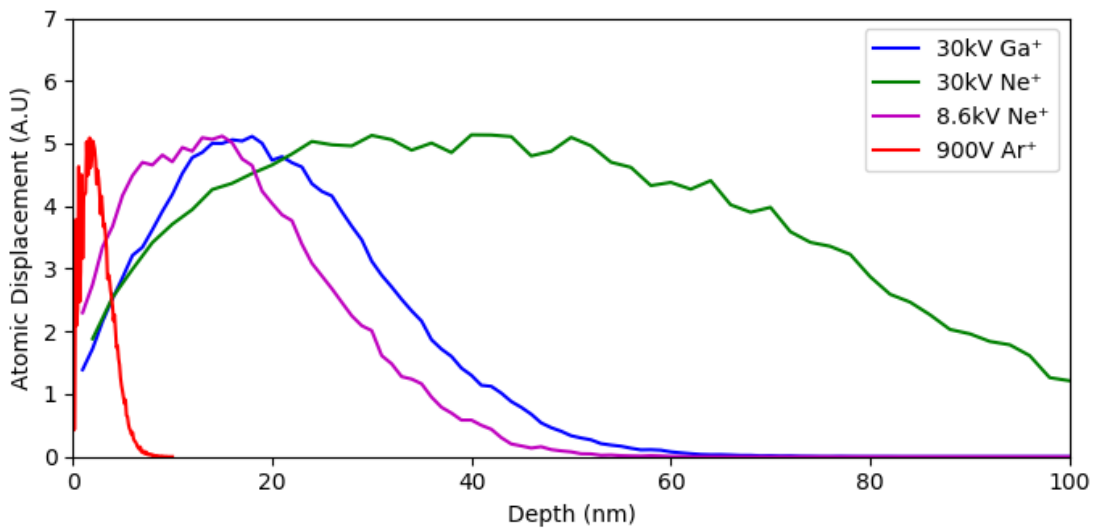
56

Figure 43: SRIM data showing atomic displacement of silicon over depth

Figure 44 is a visual representation of the displacement damage over depth with the Y-axis of depth scaled correctly to the image, again the simulated data fits quite well to experimental data.
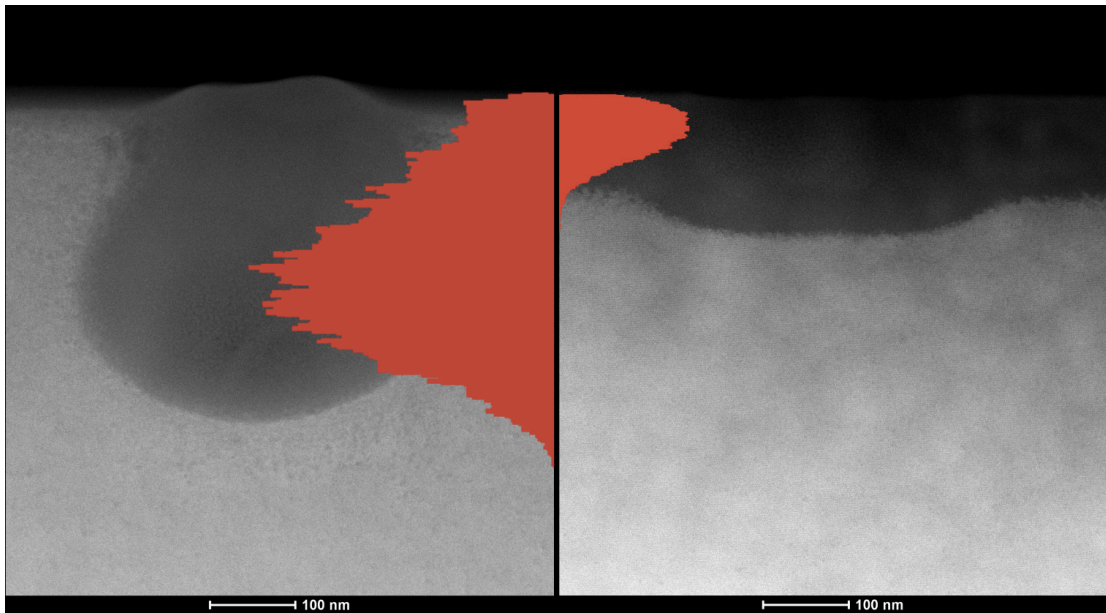

Figure 44: SRIM simulation data showing displacement per ion on the X-axis and depth on the Y-axis. The plot is overlaid on He+ ion experimental data left and Ne+ ion experimental data right.

6.9   Experiments and simulation conclusion

Sputtering is the removal of atoms at the surface when bombarded by energetic particles. If an ion travelling through the bulk has enough energy it can displace an atom it interacts with and instead of removing the atom, moves it from its current position breaking bonds with its neighbouring atoms, causing lattice disruption. From looking at the images of the different ions interacting with the bulk silicon it is obvious that the heavier Ga^+ ions are much more effective at removing material. As discussed in the ion theory section, due to gallium's larger mass and lower velocity, the Ga^+ ions don't travel as far into the bulk of the material and the Ga^+ ions have more nuclear interactions near the surface, making them effective at displacing atoms and removing material. According to literature, it is possible to use light ions such as He^+ to remove material from a surface [15] (p55), also equation eq.4 can be used calculate that a He^+ ion can transfer more than enough energy to displace a Si atom. However, from the experimental data and simulations, it appears the high-velocity light ions He^+ and Ne^+ scatter through the bulk going through a series of electronic/inelastic scattering events before finally having nuclear interactions and displacing atoms. By the time the He^+ and Ne^+ ions have slowed down they are deep into the bulk of the sample, so instead of removing material the structure of the sample is disrupted, voids are produced and swelling occurs [33]. The sub-surface damage extends hundreds of nanometres into the bulk. Although the SRIM simulations are not used in a quantitative manner, the simulations are useful to help interpret qualitatively the experimental results. The simulations show that the light ions travel deep into the bulk of the material and are scattered out in all directions creating a large volume to the interaction. the simulation helps visualise this interaction and reiterates the relationship between velocity and penetration depth discussed in the theory section

Because of the damage caused by the light ions, this limits their application in producing samples suitable for high-resolution microscopy even compared to gallium. For example, for a 100nm thick sample with a final ion beam polishing using He^+ ions, the damage would extend through the whole thickness of the sample rendering it useless for microscopy. Ne^+ ions potentially could be used for sample preparation, lowering the voltage reduces the depth of the damage. Another factor to take into account is the right sample, a heavier material will have a greater stopping power, and this will also reduce the penetration depth of the ion. Another drawback to using the NanoFab for sample preparation, from an instrumentation perspective, is the GFIS source only produces low current probes, which would make thinning large area samples very time-consuming.

7 Low Voltage Ar$^+$ ion sample preparation

With any new technology, there is a learning curve when trying to get the best from an instrument. Early attempts to use the NanoMill did not achieve the required result. One problem with the Nanomill was unwanted milling of the protective layer and occasional damaging of the area of interest at the sample interface. Figure 45 shows a lamella that has had its top surface eroded away
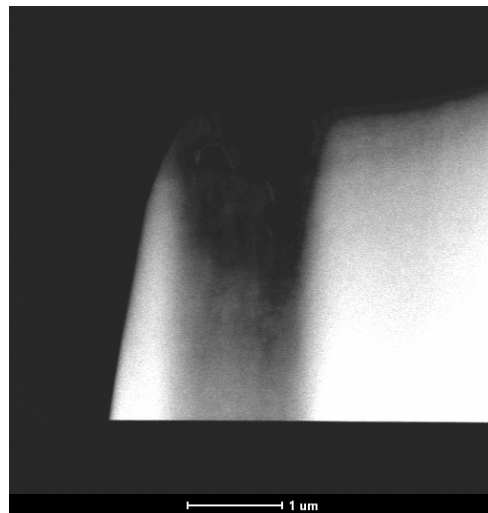

Figure 45: Lamella that has had its top surface eroded away after NanoMill polishing

A simple solution to this issue was to mount the Omniprobe grid upside down. In this configuration, the substrate is acting as protection for the area of interest. This however is only a workaround and does not ultimately fix the problem. To solve this problem a novel approach to beam scanning was used. The beam size was calculated to be ~2µm at 900V, after this simple trigonometry can be used to calculate the interaction area based on the probe size and tilt

$$\text{interaction area } = \frac{P}{\cos(90 - A)} \qquad\qquad eq.13$$

Where P is the probe size and A is the tilt angle.

If the surface of the lamella is facing towards the probe, then the interaction area is the size of the probe itself, however, if the sample is at a glancing angle as it is in this setup the

interaction area is a cross-section of the beam so the Y direction will be larger. For example, if the sample is tilted at 12°, the static probe will interact with an area 2µm x 10µm. The technique developed consists in tilting the sample more, up to about 20° for a 6µm height lamella; then mill a line in the X direction only, moving the beam in the Y direction only moves the beam off the sample. In this configuration, a static beam would interact with a 2µm x 6µm µm area; therefore, scanning the beam across 10µm in the X direction will efficiently thin a 10µm x 6µm area.
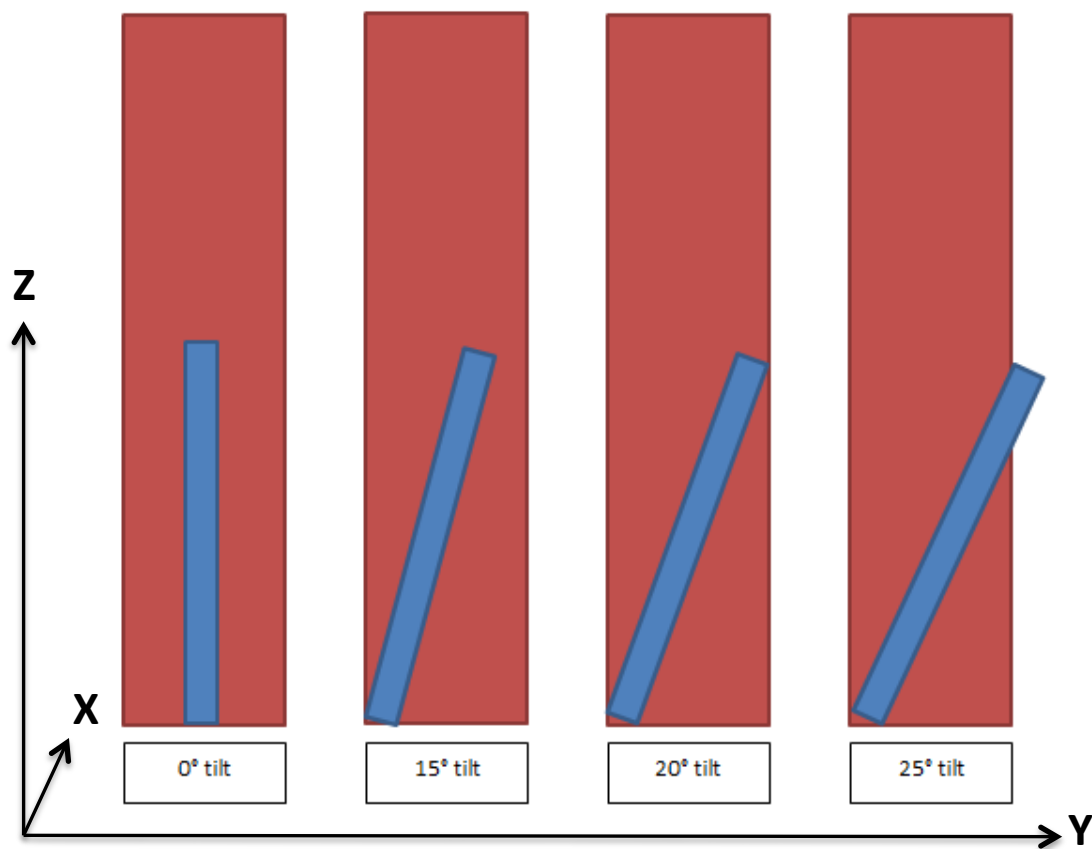

Figure 46: Diagram displaying a range of tilts based on lamella 6µm high 500nm width (Blue) and 2µm Ar$^+$ probe (Red), side view.

In the following section, we will look at some examples of samples that have been thinned using the NanoMill.

8 NanoMill results using new technique

8.1 He$^+$ ion irradiated MoS$_2$

For the first example of the technique in action, it was used to create an extremely high-quality sample for the investigation of bilayer MoS$_2$. The aim of this part of the project was to look at controlled defect engineering of the MoS$_2$ [34]. Here the changes to crystal structure and any changes to the spacing between the layers of the bilayer material are particularly important. A standard cross-section lamella was produced using a Zeiss Auriga, low voltage 5kV Ga$^+$ polishing was performed in the Auriga, all final thinning was performed using 900V Ar$^+$ in the NanoMill. Figure 47(a) shows a non-irradiated area and of the MoS$_2$ with the bilayer structure clearly visible, 47(b) shows the He$^+$ ion irradiated area under an additional amorphous hydrocarbon layer from helium ion beam induced deposition (IBID)
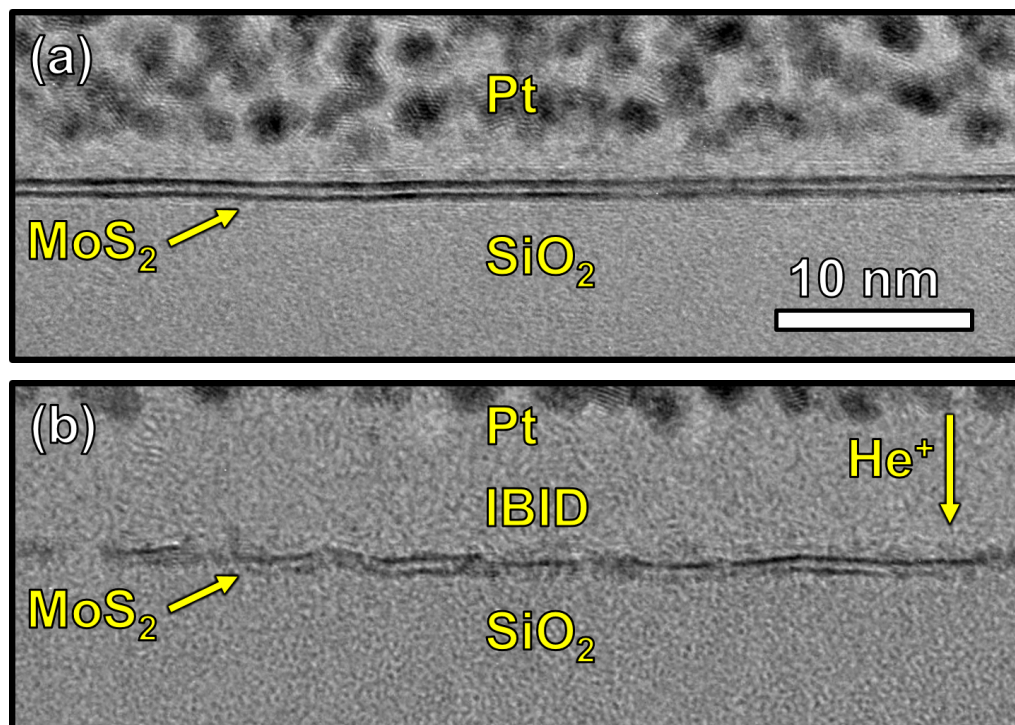

Figure 47: HR-TEM images of cross-section MoS$_2$ (a) pristine bilayer not interacted by He$^+$ ion beam; two pristine layers of MoS$_2$ clearly visible in the image (b) an area of the MoS$_2$ that has been irradiated using 6x10^{15} cm^2 He$^+$ ion beam

The bilayer structure was clearly visible allowing for spacing measurements to be made; in addition, and most importantly, the lattice disruption could be observed in HAADF STEM.
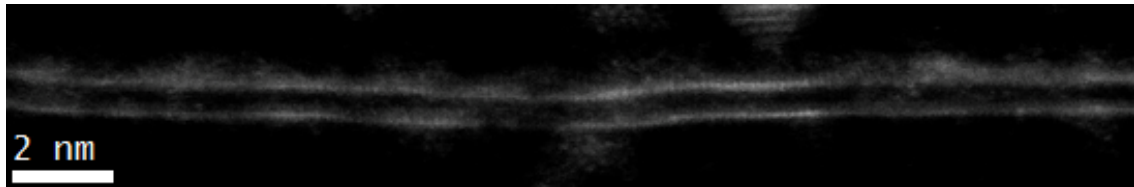
Figure 48: HR- HAADF STEM image showing lattice disruption in He^{+} irradiated area on bilayer MoS2.

The fact that we were able to obtain this level of detail from such a sample is a corroboration of the fact that it was extremely thin, otherwise we would have encountered unavoidable loss of data in the irradiated areas. To see how thin the sample was, thickness maps were performed using energy filtered TEM (EFTEM), figure 49
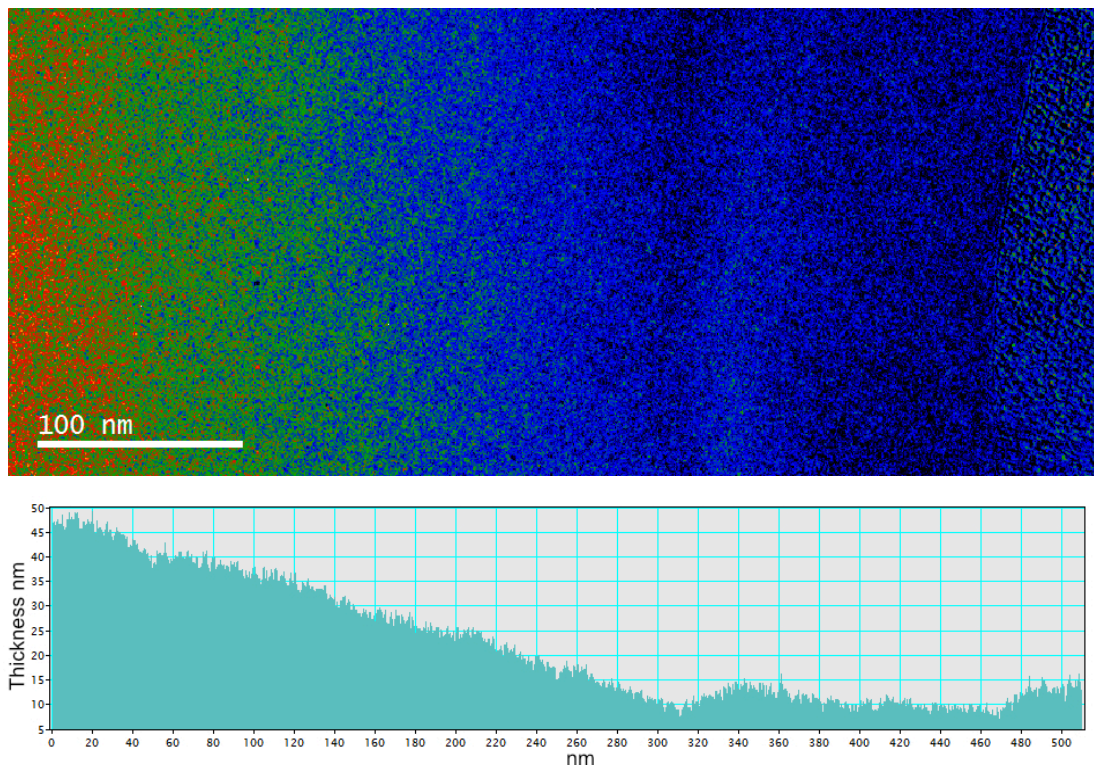

Figure 49: EFTEM thickness map and profile of the map showing absolute thickness from left to right.

EFTEM maps produce a t/λ value based on the zeroloss map and the unfiltered image, an absolute value can be calculated using the log-ratio method [35]-p294. EFTEM thickness map demonstrated that the sample was ~10nm thick in the area of interest while still maintaining structural integrity. This allowed imaging of defects on bilayer MoS$_2$ induced by He^{+} ion irradiation.

62

8.2   NAND Device

The next sample we undertook under investigation was a collaborative specimen sent by Fischione, manufacturer of the NanoMill. This sample was a NAND solid-state drive (SSD) device, which was cross-sectioned. First off, the packaging of the device was delayerd using a broad ion beam. A lamella was prepared using a 30kV FIB, 5kV polishing was also performed in the FIB. When the thickness of about 100nm was achieved, a final polishing was performed using a low voltage Ar^+ ion beam from 900V - 500V using the technique described in the Ar^+ ion milling section 7. When the sample had been thinned and polished at low voltage, imaging and spectroscopy were performed using a NION UltraSTEM 200 [36].
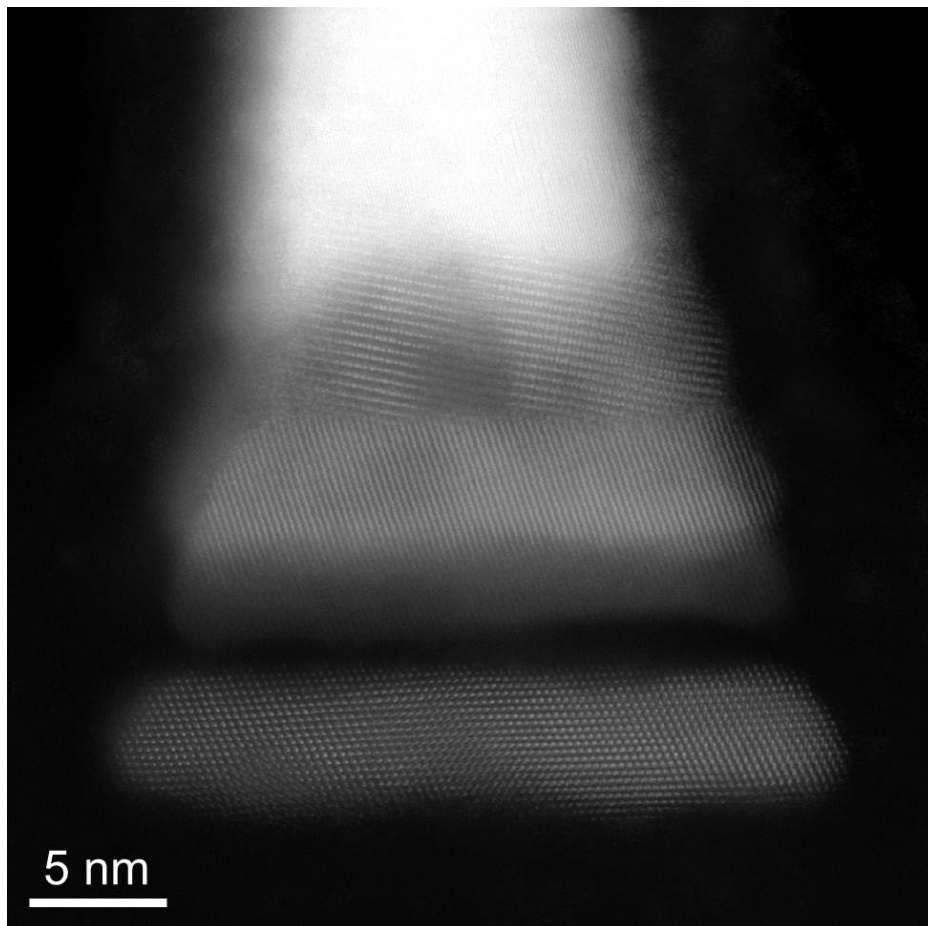

Figure 50: HR- HAADF STEM image of the NAND device.

A combination of EDX and EELS were performed to map the elements due to the overlapping peaks in EDX from the tungsten, tantalum, hafnium and silicon in the 1.64keV-1.77keV range. Elemental maps were performed at 60kV W and Ta were mapped using EDX because of a direct overlap at 36eV in EELS, Hf and Si were mapped using EELS. The only reason these elements could be mapped using EELS is because the sample was indeed extremely thin. The

peaks that were mapped are low energy peaks starting at 31eV; if the sample was too thick, plural scattering would have unavoidably caused any details to be lost in the low loss region.
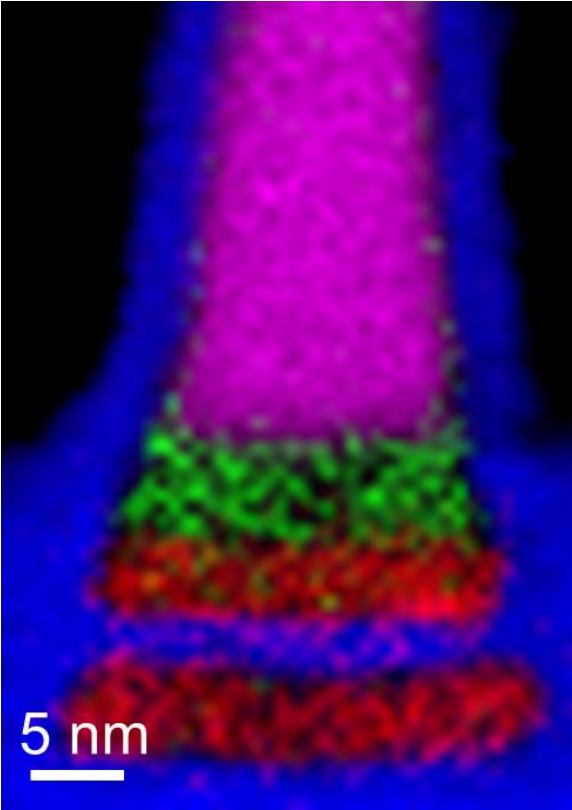

Figure 51: Combined EDS and EELS elemental maps from the multi-layer stack of the bitline structure. W in pink, Ta in green and Si in blue, Hf in red were acquired by EDS and EELS, respectively.
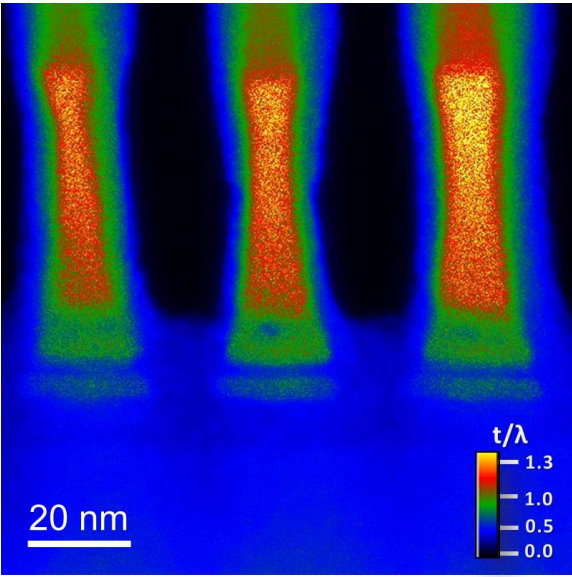

Figure 52: A t/λ thickness map of the sample performed at 60kV

From the t/λ values, the absolute thickness can be calculated. Table 2 shows a sample thickness below 20nm.

Table 2: Average specimen thickness calculated as absolute thickness, t, given the measured t/λ at 60 kV accelerating voltage.

	t/λ	Thickness, t [nm]
W	1.0	25.0
Si substrate	0.4	18.0

Preparing samples with a thickness in the order of a couple of tens of nanometres is becoming more of a necessity as our electronic devices get smaller. An important factor is to maintain the structural integrity of the sample, as it is undesired to destroy the area of interest before it has even been analysed.

8.3 Bismuth Titanate

The third example of high-resolution imaging and spectroscopy enhabled by my sample-preparation studies was a bismuth titanate sample. Imaging and analysis were performed at 60kV. This sample was originally prepared using a standard FIB lift-out procedure with 5kV Ga$^+$ final thinning. The plan was to get the sample thin enough to perform high-resolution imaging and spectroscopy at 60kV. Another motivation to get the sample extremely thin was to image defects that had occurred in the structure. Imaging a single crystal on-axis is a much easier task than a crystal with a mixed structure that is tilted off-axis. Making the sample thinner will help de-convolute the signal as the electron beam will interact with fewer layers as it passes through the sample. Figure 53 shows a clear high-resolution STEM image of the bismuth titanate. Not only is the single-crystal perovskite structure clearly visible, but the dislocations running through the structure are clearly resolved.
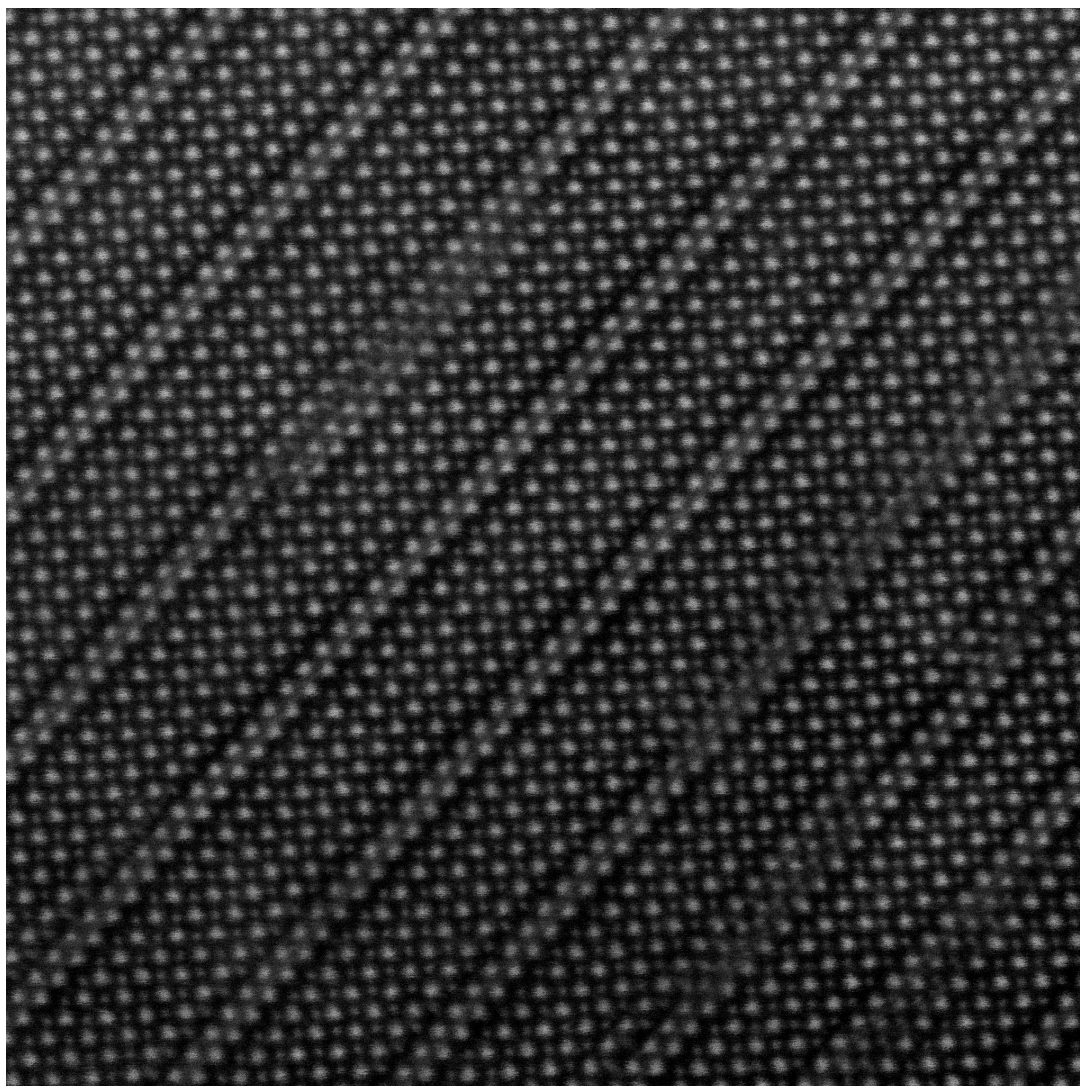
Figure 53: HR-HAADF STEM image of bismuth titanate sample performed at 60kV

Bismuth titanate is a multiferroic material when the perovskite structure is doped. In order to see where the dopants were distributed in the material, atomic resolution mapping was performed. To improve the signal to noise multiple acquisitions are summed together. Summing multiple frames is only possible if the sample remains undamaged, this would not be possible at 200kV as the analysed region starts to deteriorate after a couple of acquisitions. At 60kV many acquisitions can be performed without any damage occurring to sample allowing a high signal to noise to be achieved. Figure 54 shows high-resolution high signal to noise elemental maps. It is clear that the iron dopant is distributed within the middle three layers of the five-layer perovskite structure. A thin undamaged sample was key to obtaining this data.
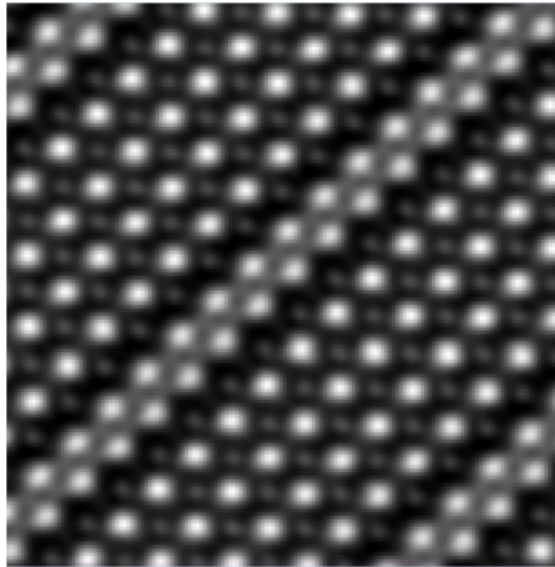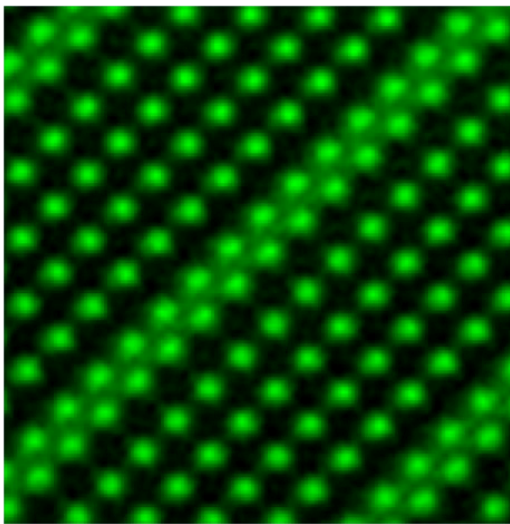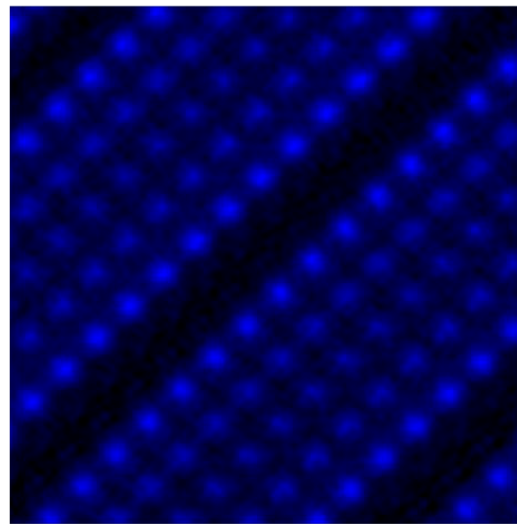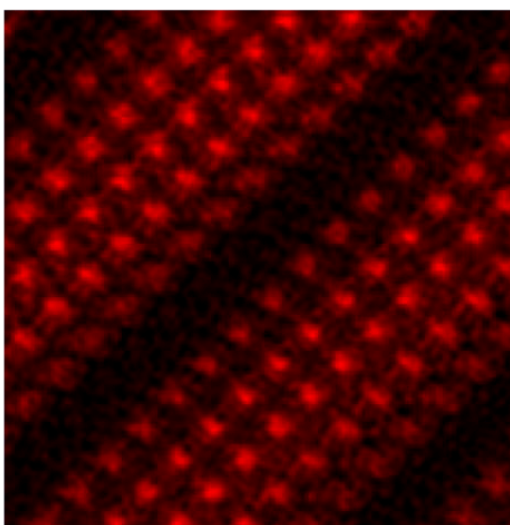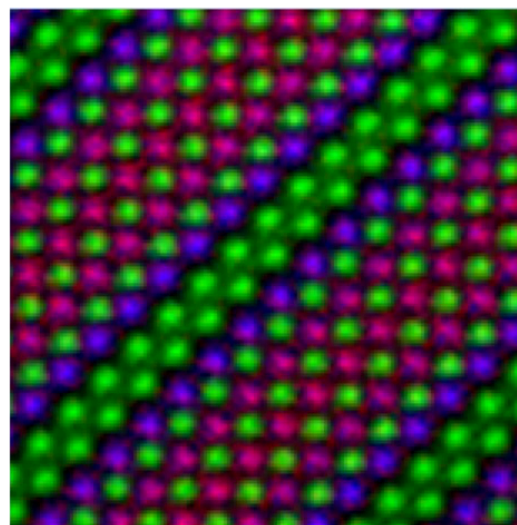
Figure 54: Atomic resolution EDX mapping of doped bismuth titanate. High signal to noise achieved by multiple acquisitions summed together producing very clear elemental maps

9 Conclusion and Future work

In this study, a range of light ion species interacting with silicon were investigated to see if they would be useful for the preparation of samples for high-resolution electron microscopy and analysis. This was achieved by analysing the cross-section of the interaction in silicon and also using simulations of the interaction. It appears that whilst He$^+$ and Ne$^+$ ions have many applications, this thesis work demonstrated that these are not the best options for final sample thinning. In contrary, low voltage Ar$^+$, when used for final polishing, successfully produced samples suitable for high-resolution analysis. We can therefore conclude that a low voltage Ar$^+$ ion beam is still a better solution for producing high-end samples. In the author's opinion, even a BIB Ar$^+$ system would be a better choice. Another big factor to take into account is cost: a high-end dual-beam FIB with low voltage capability and separate Ar$^+$ ion beam system would not cost as much as a He$^+$/Ne$^+$ ion instrument.

For future work, Xe$^+$ ions should be investigated. Several companies are producing commercially available plasma FIB instruments using a Xenon source. Xenon is a heavy inert element, using low accelerating voltage with its large mass give it the potential for localised surface sputtering and being an inert element should stop it reacting with the sample and changing its properties.

A positive outcome from this study is that a new technique was developed for the NanoMill. This allowed high-quality samples to be produced with greater efficiency. It is evident from section 8 that extremely thin defect-free samples were produced enabling clear high-resolution imaging and spectroscopy.

10 **Appendix 1:** Probe size calculation

During this project the ion beam interactions have been performed by dwelling the beam in a single spot on the surface of the of the silicon. The single spot method allows us to see the profile of the interaction and details that maybe lost scanning an area. In order to work out the ion dosage in a unit area (cm^2) first of all the probe size has to be calculated. The edge resolution technique was employed. Here the contrast change from the edge to background noise is used. The distance between 25% and 75% of the contrast drop off is measured. This value gives a good approximation of the effective probe size. [37] (p164).
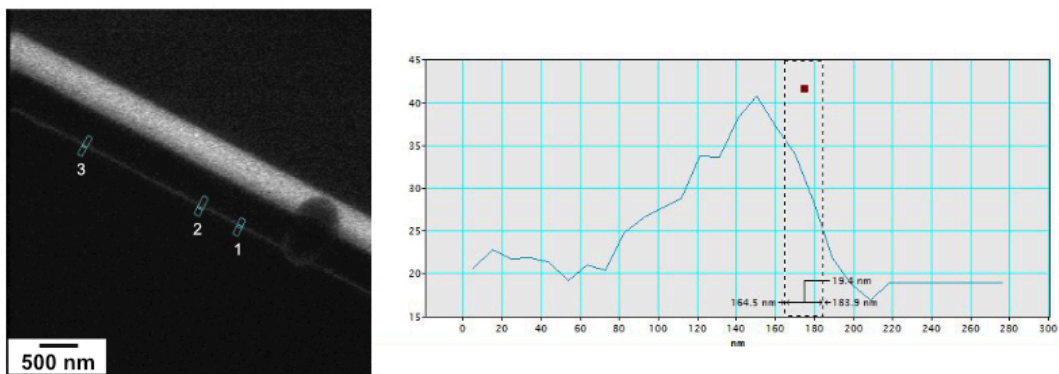
Once we have the probe diameter, current and dwell time, the ion dose per cm^2 can be calculated using equation eq.12.

$$D = \frac{(I/e)\,t}{A}$$

Where ion dose, D, is related to the beam current, I, in amps and time, t, is in seconds. e is the electron charge and A is area in cm^2.

11 Bibliography

[1]   Richard P. Feynman, "There's a Plenty of Room At the bottom," *Engineering and Science*, vol. 23. pp. 22–36, 1960.

[2]   H. . Zandbergen, C. J. . Hetherington, and R. Gronsky, "Sample preparation of YBa2Cu3O7−δ for high-resolution electron microscopy," no. July, 1988.

[3]   R. M. Langford and A. K. Petford-Long, "Preparation of transmission electron microscopy cross-section specimens using focused ion beam milling," *J. Vac. Sci. Technol. A Vacuum, Surfaces, Film.*, vol. 19, no. 5, pp. 2186–2193, 2001, doi: 10.1116/1.1378072.

[4]   L. A. Giannuzzi and F. A. Stevie, "A review of focused ion beam milling techniques for TEM specimen preparation 10_1016-S0968-4328(99)00005-0 Micron ScienceDirect_com," *Micron*, vol. 30, pp. 197–204, 1999.

[5]   J. Mayer, L. A. Giannuzzi, T. Kamino, and J. Michael, "TEM sample preparation and FIB-induced damage," *MRS Bull.*, vol. 32, no. 5, pp. 400–407, 2007, doi: 10.1557/mrs2007.63.

[6]   "ORION NanoFab - Helium Ion Microscope (HIM)." [Online]. Available: https://www.zeiss.com/microscopy/int/products/multiple-ion-beam/orion-nanofab-for-materials.html.

[7]   E. Abbe, "Beitrage zur Theorie des Mikroskops," *Arch. Mikr. Anat.*, vol. 9, pp. 413–468, 1873, doi: 10.1007/BF02956173.

[8]   Oxford Instruments, "Inca support Help Files." .

[9]   D. B. Williams and C. B. Carter, *Transmission electron microscopy: A textbook for materials science*. 2009.

[10]   E. Rutherford, "The scattering of α and β particles by matter and the structure of the atom," *London, Edinburgh, Dublin Philos. Mag. J. Sci.*, vol. 21, no. 125, pp. 669–688, May 1911, doi: 10.1080/14786440508637080.

[11]   J. J. Thomson, " XLII. Ionization by moving electrified particles ," *London, Edinburgh, Dublin Philos. Mag. J. Sci.*, vol. 23, no. 136, pp. 449–457, 1912, doi: 10.1080/14786440408637241.

[12]   M. Nastasi, J. Mayer, and J. K. Hirvonen, *Ion-Solid Interactions*, vol. 279. Cambridge University Press, 1996.

[13]   J. F. Ziegler, M. D. Ziegler, and J. P. Biersack, "SRIM - The stopping and range of ions in matter (2010)," *Nucl. Instruments Methods Phys. Res. Sect. B Beam Interact. with Mater. Atoms*, vol. 268, no. 11–12, pp. 1818–1823, 2010, doi:

10.1016/j.nimb.2010.02.091.

[14]   Y. Nan, *Focused ion beam systems: Basics and applications*, vol. 9780521831. 2007.

[15]   D. C. Joy, *Helium Ion Microscopy*. New York, NY: Springer New York, 2013.

[16]   Y. Yamamura and H. Tawara, "Energy dependence of ion-induced sputtering yields from monatomic solids at normal incidence," *At. Data Nucl. Data Tables*, vol. 62, no. 2, pp. 149–253, 1996, doi: 10.1006/adnd.1996.0005.

[17]   S. M. Sze, R. H. FOWLER, and L. NORDHEIM, "Electron Emission in Intense Electric Fields," *Semicond. Devices Pioneer. Pap.*, vol. 14, no. 1923, pp. 683–691, 1991, doi: 10.1142/9789814503464_0087.

[18]   T. Matsushita, *Electricity and Magnetism*. Tokyo: Springer Japan, 2014.

[19]   P. Grivet, "Electron Optics (2nd English Edition). By P. Grivet, translated by P. W. Hawkes and revised by A. Septier," *PERGAMON Press*, vol. 97, no. 1–2, Jan. 1973, doi: 10.1111/j.1365-2818.1973.tb03781.x.

[20]   JEOL, "lens Configuration." [Online]. Available: https://www.jeol.co.jp/en/science/sem.html.

[21]   J. I. Goldstein *et al.*, *Scanning Electron Microscopy and X-ray Microanalysis*. Boston, MA: Springer US, 2003.

[22]   L. A. Giannuzzi, *Introduction to Focused Ion Beams*, vol. 1. Boston, MA: Springer US, 2005.

[23]   Bruker, "Bruker EDX." [Online]. Available: https://www.bruker.com/products/x-ray-diffraction-and-elemental-analysis/eds-wds-ebsd-sem-micro-xrf-and-sem-micro-ct/quantax-eds-for-tem/overview.html.

[24]   Gatan, "Gatan EELS." [Online]. Available: https://eels.info/products/overview.

[25]   D. Fox, Y. Chen, C. C. Faulkner, and H. Zhang, "Nano-structuring, surface and bulk modification with a focused helium ion beam," *Beilstein J. Nanotechnol.*, vol. 3, no. 1, pp. 579–585, 2012, doi: 10.3762/bjnano.3.67.

[26]   F. Khanom, "TEM Sample Preparation using Gallium & Neon Ion Beams."

[27]   S. Tan, R. Livengood, D. Shima, J. Notte, and S. McVey, "Gas field ion source and liquid metal ion source charged particle material interaction study for semiconductor nanomachining applications," *J. Vac. Sci. Technol. B, Nanotechnol. Microelectron. Mater. Process. Meas. Phenom.*, vol. 28, no. 6, 2010, doi: 10.1116/1.3511509.

[28]   C. M. Gonzalez *et al.*, "Focused helium and neon ion beam induced etching for advanced extreme ultraviolet lithography mask repair," *J. Vac. Sci. Technol. B, Nanotechnol. Microelectron. Mater. Process. Meas. Phenom.*, vol. 32, no. 2, 2014, doi: 10.1116/1.4868027.

[29] R. Abdolvand and F. Ayazi, "An advanced reactive ion etching process for very high aspect-ratio sub-micron wide trenches in silicon," *Sensors Actuators, A Phys.*, vol. 144, no. 1, pp. 109–116, 2008, doi: 10.1016/j.sna.2007.12.026.

[30] R. P. Babu, S. Irukuvarghula, A. Harte, and M. Preuss, "Nature of gallium focused ion beam induced phase transformation in 316L austenitic stainless steel," *Acta Mater.*, vol. 120, pp. 391–402, 2016, doi: 10.1016/j.actamat.2016.08.008.

[31] V. Veligura, G. Hlawacek, R. P. Berkelaar, R. van Gastel, H. J. W. Zandvliet, and B. Poelsema, "Digging gold: Kev He+ ion interaction with AU," *Beilstein J. Nanotechnol.*, vol. 4, no. 1, pp. 453–460, 2013, doi: 10.3762/bjnano.4.53.

[32] Y. Yang, Y. G. Li, M. P. Short, C. S. Kim, K. K. Berggren, and J. Li, "Nano-beam and nano-target effects in ion radiation," *Nanoscale*, vol. 10, no. 4, pp. 1598–1606, 2018, doi: 10.1039/c7nr08116b.

[33] M. A. Lively, S. X. Bennett, and J. P. Allain, "Molecular dynamics studies of ion beam implantation and patterning of silicon: Effect of noble gas cluster formation," *Phys. Rev. B*, vol. 97, no. 23, pp. 1–13, 2018, doi: 10.1103/PhysRevB.97.235443.

[34] P. Maguire *et al.*, "Suppression of the shear Raman mode in defective bilayer MoS 2," *J. Appl. Phys.*, vol. 125, no. 6, pp. 2–6, 2019, doi: 10.1063/1.5086366.

[35] R. F. Egerton, *Electron Energy-Loss Spectroscopy in the Electron Microscope*. Boston, MA: Springer US, 2011.

[36] C.S. Bonifacio, P. Nowakowski, M.L. Ray, P.E. Fischione, C. Downing "High throughput and multiple length scale sample preparation for characterization and failure analysis of advanced semiconductor devices," in *ISTFA 2019*, 2019, vol. 1, no. 4, pp. 295–301.

[37] G. Hlawacek, *Helium Ion Microscopy*. Cham: Springer International Publishing, 2016.